Turbulent Mixing in the Red Sea Outflow Plume from a High-Resolution Nonhydrostatic Model

TAMAY M. ÖZGÖKMEN, WILLIAM E. JOHNS, HARTMUT PETERS, AND SILVIA MATT

Division of Physical Oceanography and Meteorology, Rosenstiel School of Marine and Atmospheric Science, University of Miami, Miami, Florida

(Manuscript received 1 October 2002, in final form 7 February 2003)

ABSTRACT

Given the motivation that overflow processes, which supply source waters for most of the deep and intermediate water masses in the ocean, pose significant numerical and dynamical challenges for ocean general circulation models, an intercomparison study is conducted between field data collected in the Red Sea overflow and a high-resolution, nonhydrostatic process model. The investigation is focused on the part of the outflow that flows along a long narrow channel, referred to as the ''northern channel,'' that naturally restricts motion in the lateral direction such that the use of a two-dimensional model provides a reasonable approximation to the dynamics. This channel carries about two-thirds of the total Red Sea overflow transport, after the overflow splits into two branches in the western Gulf of Aden. The evolution of the overflow in the numerical simulations can be characterized in two phases: the first phase is highly time dependent, during which the density front associated with the overflow propagates along the channel. The second phase corresponds to that of a statistically steady state. The primary accomplishment of this study is that the model adequately captures the general characteristics of the system: (i) the gradual thickening of the overflow with downstream distance, (ii) the advection of high salinity and temperature signals at the bottom along the channel with little dilution, and (iii) ambient water masses sandwiched between the overflow and surface mixed layer. To quantify mixing of the overflow with the ambient water masses, an entrainment parameter is determined from the transport increase along the slope and is expressed explicitly as a function of mean slope angle. Bulk Richardson numbers are estimated both from data and model and are related to the entrainment parameter. The range of entrainment parameter and its functional dependence on bulk Richardson number in this study are found to be in reasonable agreement with those reported from various laboratory experiments and that based on measurements of the Mediterranean overflow. The results reveal a complex dynamical interaction between shear-induced mixing and internal waves and illustrate the high computational and modeling requirements for numerical simulation of overflows to capture (at least in part) turbulent transports explicitly.

1. Introduction

Cooling in polar seas (e.g., Dickson et al. 1990; Borenäs and Lundberg 1988) and evaporation in marginal seas (e.g., the Mediterranean Sea; Baringer and Price 1997a) lead to the formation of dense water masses that are released into the large-scale ocean circulation in the form of overflows, which are bottom gravity or density currents. For instance, intense evaporation in the Mediterranean Sea produces salty water that sinks to the bottom, flows over the sill in the Strait of Gibraltar (Bryden and Kinder 1991), and forms a bottom density current that descends along the continental slope. The Mediterranean water is dense enough that it would sink to the bottom of the Atlantic Ocean if it did not undergo mixing and dilution. However, observations show that the Mediterranean salinity tongue spreads across the North Atlantic basin at middepths (Lozier et al. 1995) because it is diluted by entrainment of the overlying fresh Atlantic water (e.g., Price et al. 1993). Similar considerations apply to other overflows such as the Red Sea overflow (Murray and Johns 1997), which is the focus of the present study. Most of the deep and intermediate water masses in the ocean have their origin in these overflows from high-latitude and marginal seas (Price and Baringer 1994). A systematic comparison between several realistic ocean circulation models for the North Atlantic circulation demonstrated that the strength of the large-scale thermohaline circulation is strongly sensitive to the representation of overflows in these models (Willebrand et al. 2001). Therefore, overflows are intimately linked to the ocean's role in climate dynamics. Other impacts include formation of pronounced upper-ocean currents due to modification of potential vorticity by persistent and localized mixing of overflows with ambient water masses (Jia 2000; Özgökmen et al. 2001; Özgökmen and Crisciani 2001).

Corresponding author address: Dr. Tamay M. Özgökmen, RSMAS, University of Miami, 4600 Rickenbacker Causeway, Miami, FL 33149-1098.
E-mail: tamay@rsmas.miami.edu

© 2003 American Meteorological Society

Since our ability to predict the behavior of large-scale ocean circulation relies primarily on the accuracy of ocean models, it is important that such models represent accurately the dynamics of overflows, in particular their mixing with the ambient fluid.

Most of the modeling efforts regarding overflows are presently focused on improving their downslope flow, since in coarse-resolution (horizontal grid size of 100 km) geopotential vertical coordinate models typically employed in climate studies, the volume of ambient water mass at each topographic step can exceed the volume of overflows. Such inadequate discretization can lead to the artificial dilution of overflows and prohibit their downslope flow (e.g., Beckmann and Döscher 1997; Winton et al. 1998; Killworth and Edwards 1999; Nakano and Suginohara 2002). Another fundamental issue is an accurate representation of the mixing of overflows with ambient water masses, a process that determines the properties of intermediate and deep water masses in the ocean. It is generally accepted from laboratory experiments (Simpson 1969) and observations (e.g., Baringer and Price 1997b) that mixing between density currents and the ambient fluid takes place primarily via the shear instability. Overflows have a small vertical scale, typically 100–300 m (Price and Yang 1998). The embedded overturns are even smaller, reaching at most 30 m in thickness, owing to limitations imposed by stable stratification (Peters et al. 2002). An explicit representation of mixing in overflows in numerical models requires not only a small vertical grid scale, but also a horizontal grid scale that is small enough to capture the billows forming near the density interface. Oceanic observations indicate that the typical height-to-length ratio of Kelvin–Helmholtz billows is about 0.1 (e.g., Marmorino 1987). The typical resolution requirements for explicit resolution of billows are 10–30 m in the vertical direction and 100–300 m in the horizontal direction. Because overflows propagate with speeds $O(1\ \mathrm{m\ s^{-1}})$, the timescale for the evolution of billows is $O(100\ \mathrm{s})$. Such small spatial and timescales are computationally prohibitive in large-scale ocean models at the present time. More fundamentally, most ocean models are based on hydrostatic primitive equations. According to the hydrostatic approximation, the primary dynamical balance in the vertical momentum equation is between the pressure gradient and gravitational acceleration terms. Therefore, vertical acceleration terms are omitted, which lead to misrepresentation of vertical mixing processes that are of importance in the dynamics of overflows. Therefore, parameterizations are needed in ocean circulation models to represent the mixing of overflows with the ambient water masses.

A prerequisite to the development of such parameterizations is a good understanding of the dynamics of bottom gravity currents. The present level of our systematic understanding is primarily derived from laboratory tank experiments (Ellison and Turner 1959; Simpson 1969; Britter and Linden 1980; Simpson 1982; Turner 1986; Simpson 1987; Hallworth et al. 1996; Monaghan et al. 1999; Baines 2001). However, when configured for the small slopes of observed overflows [$O(1^\circ)$], the dense source fluid cannot accelerate enough within the bounds of typical laboratory tanks [$O(1\ \mathrm{m})$] so that it exhibits a turbulent behavior. For turbulence to occur, laboratory experiments are configured with slopes greater than 10°. It is also difficult to maintain a complex ambient stratification in these tanks. While a favorable agreement has been obtained between some laboratory results and idealized geophysical-scale numerical simulations of bottom gravity currents (Özgökmen and Chassignet 2002), there is a wide gap between bottom gravity currents in the laboratory and overflows in the ocean in terms of the range of scales and the complexity of processes.

A comprehensive observational program of the Red Sea overflow, the Red Sea Outflow Experiment (REDSOX; Bower et al. 2002; Johns et al. 2002; Peters et al. 2002), provides an oceanic dataset that is ideally suited to tackle the computational and modeling challenge of accurately reproducing the distribution of the observed water masses and to improve our understanding of the dynamics of oceanic overflows.

The primary objective of the present investigation is to achieve an accurate representation of the observed water mass distribution in the Red Sea outflow via numerical simulation by addressing the numerous modeling challenges described above. This paper reports a model–data comparison of the part of the Red Sea outflow that flows along a long narrow channel, referred to as the ''northern channel,'' which naturally restricts motion in the lateral direction such that the use of a two-dimensional model provides a good first-order approximation to the dynamics. This channel carries about two-thirds of the total Red Sea overflow transport, after the overflow splits into two in the western Gulf of Aden. A two-dimensional, high-resolution, nonhydrostatic model is forced with temperature and salinity profiles from a survey cruise performed in February 2001 (REDSOX-1) at the inlet to the channel, and with radiation boundary conditions at the other end, with the objective of simulating and approximating the interior dynamics.

The evolution of the overflow in the numerical simulations can be characterized in two phases: the first phase is highly time dependent, during which the density front associated with the overflow propagates along the channel. The second phase corresponds to that of a statistically steady state. In this phase, the model solution is compared with the temperature and salinity profiles from REDSOX-1 cruise stations and is found to exhibit good agreement. The general flow characteristics and descent speed of the overflow also compare well with that from observations. To quantify mixing of the overflow with the ambient water masses, an entrainment parameter is determined from the transport increase along the slope and is expressed explicitly as a function of mean slope angle. Bulk Richardson numbers are es-

timated both from data and model and are related to the entrainment parameter. The range of entrainment parameter and its functional dependence on bulk Richardson number in this study are found to be in reasonable agreement with those reported from various laboratory experiments and that based on measurements of the Mediterranean overflow.

The paper is organized as follows: In section 2, the REDSOX observational program is briefly described and the area of focus is outlined. In section 3, the numerical model is introduced. The experimental setup and parameters are outlined in section 4. Results are presented in section 5. Last, we summarize and conclude in section 6.

2. REDSOX and the study area

The Red Sea Water originates in the northern Red Sea due to an excess of evaporation over precipitation (Morcos 1970; Sofianos et al. 2002). It enters the Gulf of Aden in the northwestern Indian Ocean as a salty, dense overflow through the shallow Bab el Mandeb Strait (Fig. 1, top). Early surveys of the area (Siedler 1969) and more recent studies (Fedorov and Meschanov 1988; Murray and Johns 1997) have shown that the Red Sea outflow splits into two channels, called the ''northern'' and the ''southern'' channels, as it flows into the Gulf of Aden (Fig. 1, bottom). It is observed that the northern channel, with its more confined topography, carries very high salinity water downslope and seems to allow less mixing with ambient water masses than the broader southern channel. These studies have shown that the Red Sea outflow is different from outflows in the Atlantic in the sense that it exhibits strong seasonal variability with the outflow being much weaker in the summer than in the winter.

Following up on these findings, REDSOX, a joint effort between the University of Miami's Rosenstiel School of Marine and Atmospheric Science and the Woods Hole Oceanographic Institution, provides a comprehensive description of the pathways, structure, and variability of the descending outflow plumes from the Red Sea and a better understanding of mixing and spreading processes in dense overflows. The fieldwork was carried out in two cruises during 2001, one in the winter (REDSOX-1) and one in the summer (REDSOX-2), which were timed to coincide with the periods of maximum and minimum deep outflows, respectively. The surveys consisted of three main components. First, a high-resolution hydrographic and direct current survey of the western Gulf of Aden between the Strait of Bab el Mandeb and the Tadjoura Rift was conducted using a total of 238 conductivity–temperature–depth (CTD) and direct velocity stations to describe the three-dimensional water property distributions and circulation characteristics. Second, direct measurements of turbulent mixing were made using bottom-mounted acoustic Doppler current profiler (ADCP) moorings to study the bottom stress and mixing processes in descending plumes. Third, acoustically tracked drifters were launched to observe the rates and pathways of Red Sea outflow spreading in the entire Gulf of Aden. For a comprehensive description of the observational results from REDSOX, the reader is referred to Bower et al. (2002), Johns et al. (2002), Peters et al. (2002), and REDSOX-1 cruise report (see online at http://www.rsmas.miami.edu/personal/h.peters/RSX1-report.pdf).

In the present investigation, we consider data from the REDSOX-1 cruise during the season of maximum outflow in winter and focus on the northern channel, which is approximately 100 km long, but reaches a width of only 3 km at the overflow depth (Fig. 1, bottom). In comparison, the radius of deformation of the overflow layer estimated from $R_d \approx \sqrt{g'h}/f_0 \approx 50$ km, where $g' \approx 0.014$ m s^{-2} is the reduced gravity resulting from a temperature difference of 6°C and a salinity difference of 4.3 psu from the ambient, $h = 150$ m is the overflow thickness, and $f_0 = 3 \times 10^{-5}\ s^{-1}$ is the Coriolis frequency at 12°N. Therefore, the overflow is strongly constrained by channel topography in the lateral direction, leading to the use of a two-dimensional model described in the following section. These natural simplifications make the Red Sea overflow in the northern channel an ideal, yet important case to study.

3. Approach

a. Model philosophy

Overflows have been traditionally investigated using so-called streamtube models. These models have been useful in examining the path and bulk properties of the Denmark Strait overflow (e.g., Smith 1975), Weddell Sea overflow (Killworth 1977), the Mediterranean overflow (Baringer and Price 1997b), and initial studies of the Red Sea overflow (Bower et al. 2000). Various simplifications are required in these models, such as steady state, motionless ambient fluid, simple topography, and mixing parameterization based on laboratory experiments. In recent years, there have been a number of studies employing more complex models. Jungclaus and Backhaus (1994) used a primitive equation, two-dimensional (x, y) shallow-water model with reduced-gravity approximation in the vertical. They conducted idealized experiments to investigate the effects of bottom friction and topography and also applied their model to the Denmark Strait overflow. Özsoy et al. (2001) used the same model in the analysis of the dense water plume entering the Black Sea through the Bosphorus and concluded that the slope and finescale features of the bottom topography are crucial elements in determining plume behavior. Gawarkiewicz and Chapman (1995) used a three-dimensional hydrostatic model to explore the development of a plume with negative buoyancy. They found that the leading edge of the plume forms eddies in the horizontal plane and concluded that

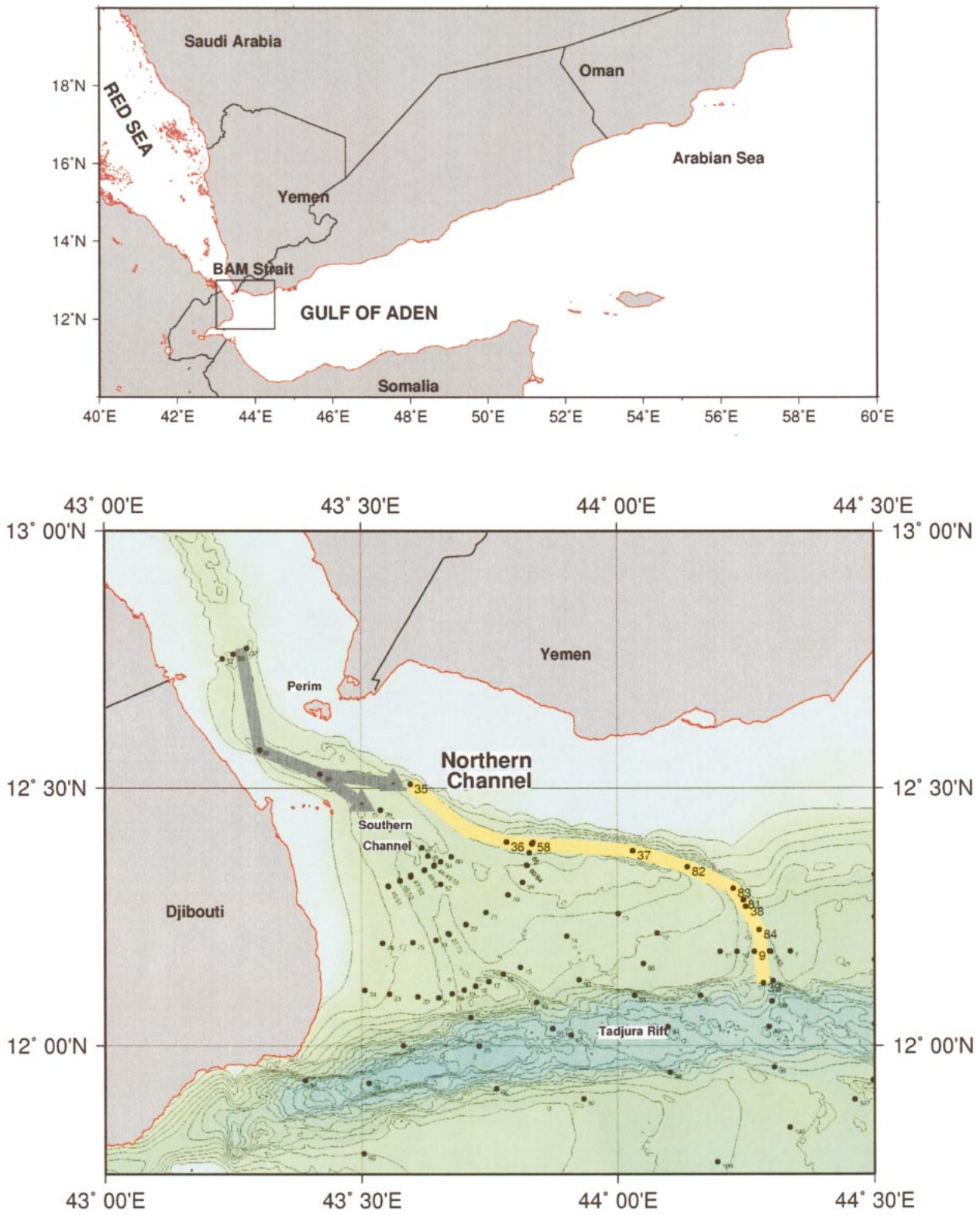

FIG. 1. (top) Chart showing the geographical location of the Red Sea, the Bab el Mandeb (BAM) Strait, and the Gulf of Aden. (bottom) Schematic depiction of the splitting of the Red Sea outflow into two branches flowing into the southern and northern (highlighted) channels, and locations of plume survey stations from REDSOX-1 cruise.

instabilities and eddy fluxes are important mechanisms for the transport of dense waters, in contrast to the quasi-steady behavior implied from streamtube models. This conclusion is also supported by numerical studies by Jiang and Garwood (1995, 1996), who used a different three-dimensional, hydrostatic, sigma-coordinate model. Jiang and Garwood (1998) concluded that topographic variations induce significant changes in the mixing and entrainment between density currents and ambient fluid. Sigma- and isopycnic-coordinate ocean general circulation models have been used to simulate the Mediterranean overflow (Jungclaus and Mellor 2000; Papadakis et al. 2003) employing various mixing parameterizations (Mellor and Yamada 1982 and Hallberg 2000, respectively).

These modeling studies have led to a significant understanding of bottom density currents in the ocean. However, none of the aforementioned studies explicitly resolve and capture the interplay between shear instability and internal waves, which lead to mixing and entrainment in overflows. This is either due to the fact that the chosen model was not able to handle such dynamics (e.g., hydrostatic approximation; inability of density interfaces to roll) and/or that the horizontal grid scale, typically *O*(few kilometers), was not sufficiently small to resolve the scales of such motion.

In this paper, we use an alternative approach to the previous modeling studies of overflows and use a high-resolution, nonhydrostatic model. Since the width of the Red Sea overflow in the northern channel is much smaller than the radius of deformation and the channel length, the effects of baroclinic instability and rotation on the flow are small, and the overflow dynamics are approximated as two-dimensional. In the absence of rotation, the mixing characteristics due to shear instability are similar in two and three dimensions (e.g., Lesieur 1997) and a two-dimensional approach to the dynamics of bottom gravity currents is supported by the laboratory experiments of Huppert (1982), Britter and Simpson (1978), Simpson and Britter (1979), Hacker et al. (1996), and numerical experiments by Härtel et al. (2000), which show that the billows in nonrotating gravity currents have a predominantly two-dimensional structure. Other three-dimensional artifacts, such as edge effects and intrusions from canyon walls, are neglected here, and the investigation of these issues requires a fully three-dimensional approach.

b. The numerical model

The governing equations of motion for an incompressible, Boussinesq fluid in two dimensions are nondimensionalized as

$$\psi = \nu_x \psi^*, \qquad (x, z) = h(x^*, z^*),$$
$$S = S^* \Delta S, \qquad T = T^* \Delta T, \tag{1}$$

where ψ is the streamfunction in the (x, z) plane, ν_x is the horizontal viscosity, h is the thickness of the overflow, and ΔS and ΔT are the ranges of salinity and temperature in the system. The asterisks are dropped, and the equations for the transport of vorticity, temperature, salinity, and conservation of mass become

$$\frac{\partial \zeta}{\partial t} + J(\psi, \zeta) = \mathrm{Ra}\left(R_\rho \frac{\partial T}{\partial x} - \frac{\partial S}{\partial x}\right) + \frac{\partial^2 \zeta}{\partial x^2} + \frac{\partial}{\partial z}\left(r \frac{\partial \zeta}{\partial z}\right) - \kappa^{\mathrm{out}}(\zeta - \zeta^{\mathrm{out}}) \tag{2}$$

$$\frac{\partial T}{\partial t} + J(\psi, T) = \mathrm{Pr}_T^{-1}\left[\frac{\partial^2 T}{\partial x^2} + \frac{\partial}{\partial z}\left(r \frac{\partial T}{\partial z}\right)\right] - \kappa^{\mathrm{in,out}}(T - T^{\mathrm{in,out}}) \tag{3}$$

$$\frac{\partial S}{\partial t} + J(\psi, S) = \mathrm{Pr}_S^{-1}\left[\frac{\partial^2 S}{\partial x^2} + \frac{\partial}{\partial z}\left(r \frac{\partial S}{\partial z}\right)\right] - \kappa^{\mathrm{in,out}}(S - S^{\mathrm{in,out}}) \tag{4}$$

$$\zeta = \nabla^2 \psi, \tag{5}$$

where $\mathrm{Ra} \equiv (g\beta\, \Delta S h^3)/\nu_x^2$ is the Rayleigh number, the ratio of the strengths of buoyancy forcing to viscous drag; $g = 9.81$ m s^{-2} is the gravitational acceleration, $R_\rho \equiv \alpha\, \Delta T/\beta\, \Delta S$ is the density ratio, quantifying the relative influences of temperature and salinity on density ($R_\rho < 1$ for bottom gravity currents), where α is the temperature expansion coefficient and β is the salinity contraction coefficient for seawater in the linear equation of state $\rho = \rho_0(1 - \alpha\, \Delta T + \beta\, \Delta S)$, $r \equiv \nu_z/\nu_x = K_{Tz}/K_{Tx} = K_{Sz}/K_{Sx}$ is the ratio of vertical to horizontal diffusivities, $Pr_T \equiv \nu_x/K_{Tx}$ and $Pr_S \equiv \nu_x/K_{Sx}$ are the temperature and salinity Prandtl numbers, superscripts "in" and "out" denote inflow and outflow profiles, and k is the relaxation frequency toward these profiles. Here,

$$J(a, b) = \frac{\partial a}{\partial x}\frac{\partial b}{\partial z} - \frac{\partial b}{\partial x}\frac{\partial a}{\partial z}$$

is the Jacobian and

$$\nabla^2 = \frac{\partial^2}{\partial x^2} + \frac{\partial^2}{\partial z^2}$$

is the Laplacian.

The prognostic equations (2)–(4) are advanced in time using a predictor–corrector type leapfrog method (Gazdag 1976). The Jacobian operator is computed using the formulation proposed by Arakawa (1966) that conserves kinetic energy and enstrophy, while accurately maintaining the symmetry property $J(a, b) = -J(b, a)$. All other differential operators are approximated by central differences. The diagnostic equation (5) is inverted using a fast Fourier transform solver (Swarztrauber 1977).

The numerical model is based on code previously employed in microscale double-diffusive convection studies (Özgökmen et al. 1998; Özgökmen and Esenkov 1998) and simulation of bottom gravity currents in com-

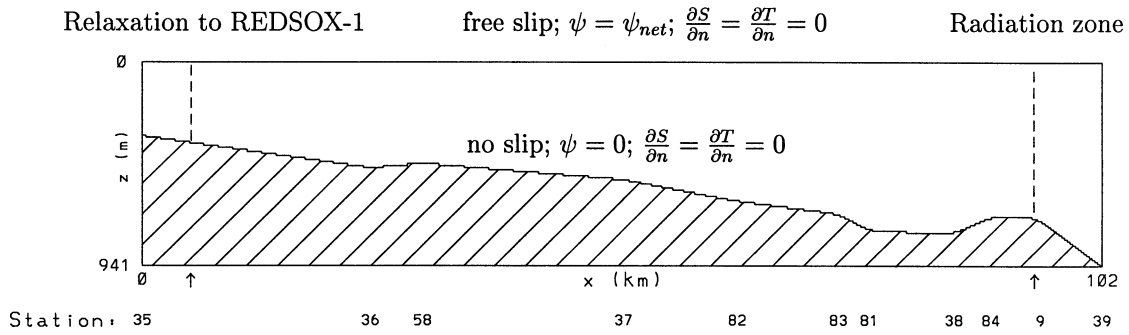

FIG. 2. Schematic illustration of model domain size, topography, locations, and numbers of REDSOX-1 survey stations and boundary conditions. The dashed lines (and arrows at the bottom) mark the extent of the relaxation zones toward REDSOX-1 data and radiation conditions near the inlet (left) and exit (right) boundaries.

parison with those from laboratory experiments (Özgökmen and Chassignet 2002). The modification of the code for the Red Sea overflow experiments was carried out on a 600-MHz Alpha workstation. The code was then parallelized using OpenMP and the production experiments were performed on a shared-memory 2 × 2.2 GHz Xeon workstation. With the model setup described in the following, the ratio of simulated time to real time is ~2 on the Alpha and ~12 on the Xeon workstations, respectively.

4. Model setup and parameters

The model is configured for the northern outflow channel beginning at Station 35 at the channel entrance and extending to Station 39 at the channel exit (Fig. 1b). The domain is 102 km long and has a maximum depth of 941 m. The bottom topography is estimated by linear interpolation between 11 survey stations within the extent of the domain and it is complex with a pronounced topographic bowl between Stations 83 and 84 (Fig. 2). The domain is discretized by a regular grid of 1401 × 101 points, which corresponds to a grid spacing of 9.41 m in the vertical and 73 m in the horizontal directions. This grid spacing is small enough to make the mixing induced by the step topography negligible. One criterion for ''slope resolving'' discretization is $\Delta x = \Delta z/\tan\theta$ (Winton et al. 1998). Using the average bottom slope angle of $\theta \approx \frac{1}{3}°$, this criterion gives $\Delta x =$ 1600 m. A smaller horizontal grid size gives a better resolution of the dynamics within the topographic step provided that the vertical grid scale is small enough, hence the 73-m horizontal grid scale used in this study. In addition, the volume/depth of light fluid at the corner of each topographic step must be much less than the volume/depth of the descending dense overflow. In our simulations, the ratio of the area of ''step water'' to the area of the overlying overflow is typically $O(10^{-2})$. Therefore, such artificial mixing is small during the initial propagation of the density front and is negligible for the simulations carried out in this study, which are integrated much longer than the timescale of propagation of the overflow throughout the domain. The propagation speed of the density front is $U_F \approx B^{1/3}$, where $B = g'Q^{\text{in}}$ is the buoyancy flux at the inlet (Britter and Linden 1980; Monaghan et al. 1999). Based on observations, $g' \approx 0.014$ m s^{-2} and the volume flux/width $Q^{\text{in}} \approx 150$ m^2 s^{-1}, and $U_F \approx 1$ m s^{-1}. Therefore, the time scale of the overflow to flow down the length of the channel is about 1 day, and the integrations are carried out for 10 days.

The experimental strategy is as follows: by forcing the model using observed temperature and salinity profiles at the inlet and by applying open boundary conditions at the exit, the objective is to approximate the interior solution. The model is driven by relaxing model temperature and salinity profiles at the inlet toward observed temperature and salinity profiles from Station 35 [$T^{\text{in}}(z)$, $S^{\text{in}}(z)$] in the first 5 km of the domain. Radiation conditions are applied from Station 9 to 39. Therefore, some interesting processes that take place near this location, such as separation of the overflow from the bottom (Johns et al. 2002; Peters et al. 2002), are not included in this study and will be subject of a future investigation. Exit temperature, salinity, and vorticity profiles [$T^{\text{out}}(x, z, t)$, $S^{\text{out}}(x, z, t)$, $\zeta^{\text{out}}(x, z, t)$] are calculated by time averaging model T, S, ζ within the 7-km extent of the exit radiation zone. The averaging period is 0.5 h, during which perturbations propagate over a distance (typically 1–2 km) that is less than the extent of the radiation zone. The relaxation frequency is on the order of the propagation time of perturbations throughout the domain, $O(1\ \text{day}^{-1})$, at the inlet, and on the order of propagation time of perturbation in the radiation zone, $O(1\ \text{h}^{-1})$ at the exit. Also, $\partial\zeta/\partial x = \partial S/\partial x = \partial T/\partial x = 0$ is applied at inlet and exit boundaries. Animations of the numerical simulations indicate that the incoming perturbations are effectively absorbed by the radiation zone, and waves are not reflected back into the model domain.

At the surface and bottom, zero flux conditions are applied to salinity and temperature $\partial S/\partial \mathbf{n} = \partial T/\partial \mathbf{n} = 0$, where $\mathbf{n}$ is the normal direction to the boundaries. A net transport also has to be specified which was esti-

mated by vertically integrating the observed velocity profiles at the along-channel stations. The integrated transport at Station 35 was 105 $m^2\ s^{-1}$ and transport values ranged from 80 to 120 $m^2\ s^{-1}$ for other stations along the channel. These values include effects due to tides, time dependence, and three-dimensionality in the upper ocean. A methodology to deal with these complications is beyond the scope of the present study. The net transport is taken equal to the value at the most constrained location by shallow water depth, that is, $\psi_{\text{net}} = 105\ m^2\ s^{-1}$ estimated from Station 35 at the domain inlet. A free-slip boundary condition is applied at the surface, and no-slip boundary condition at the bottom.

The Prandtl numbers are well known at the microscale ($\text{Pr}_T \approx 10$ and $\text{Pr}_S \approx 700$), but these values are not well defined for larger scales. Preliminary bulk estimates of these coefficients from dissipation measurements in the Red Sea outflow plume indicate that eddy viscosity is typically higher than eddy diffusivity. It is generally assumed in modeling studies that eddy viscosity is about an order of magnitude greater than eddy diffusivity (e.g., Large 1998). Therefore $\text{Pr}_T = \text{Pr}_S = 10$ is used in the following simulation (microscale double diffusive processes are suppressed at this grid scale). Experiments conducted in the range of $7 \leq \text{Pr} \leq 15$ did not show high sensitivity. The density ratio is calculated from a thermal expansion coefficient of $\alpha = 2.4 \times 10^{-4}\ ^\circ\text{C}^{-1}$ and saline contraction coefficient $\beta = 9 \times 10^{-4}\ \text{psu}^{-1}$ estimated in the temperature range of 14.5–25.5 °C and the salinity range of 35.6–39.9 psu (Millero et al. 1976) from REDSOX-1 data in the model domain.

The diffusivity ratio r should be on the $O(\Delta z^2/\Delta x^2)$ such that vertical and horizontal diffusion terms are of comparable magnitude in (2)–(4). In general horizontal processes have a larger scale than vertical processes, $\Delta x \gg \Delta z$ and $r \ll 1$ in most oceanic simulations. Here, $\Delta x/\Delta z = O(10)$ and $r = O(10^{-2})$. We have experimented both with constant r and also one that depends on the local gradient Richardson number $\text{Ri}_g = [(-g/\rho_0)(\partial\rho/\partial z)]/(\partial u/\partial z)^2$. The concept of a Ri_g-dependent vertical mixing coefficient is implied by the strong dependence of mixing in stratified fluids on Ri_g (e.g., review by Fernando 1991). Such empirical relationship is also consistent with laboratory experiments of bottom gravity currents (e.g., Ellison and Turner 1959) and with REDSOX-1 observations, in which a two-layer overflow structure is maintained by a high Richardson number ($\text{Ri}_g > 1/4$) interface coinciding approximately with the velocity maximum (Peters et al. 2002). This observation is adopted in the numerical simulations by increasing diffusivity ratio, thereby reducing the eddy-induced vertical momentum and property exchange when $\text{Ri}_g > 1/4$. In applying this to the present experiments, we take the diffusivity ratio to have the specific form

$$r(x, z, t) = r_0\{1 + (r_{\max} - 1)\ \exp[-\text{Ri}_g^{-1}(x, z, t)]\}$$

in which the diffusivity ratio is kept at a minimal value $r = r_0$ for $\text{Ri}_g \leq 1/4$, and gradually amplified by a factor of $r_{\max}$ as the Ri_g increases ($r \to r_0 r_{\max}$ for $\text{Ri}_g \to \infty$: see Fig. 3). As $r = O(10^{-2})$ from above considerations, we take $r_0 = 0.2 \times 10^{-2}$ and $r_{\max} = 8$ such that $0.2 \times 10^{-2} \leq r \leq 1.6 \times 10^{-2}$. Experiments with $5 \leq r_{\max} \leq 20$ did not exhibit sensitivity. The diffusivity ratio is updated at every model time step and grid point. The resulting range of vertical diffusivities is listed in Table 1. (The magnitude of these diffusivity coefficients do not quantify the effective mixing in the model, which is accomplished by turbulent transport).

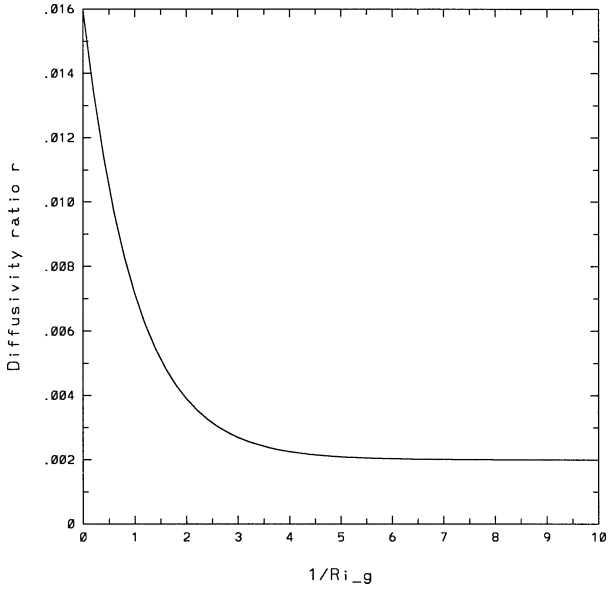

FIG. 3. Richardson number–dependent diffusivity ratio employed in the model simulations, $r = r_0\ [1 + (r_{\max} - 1)\exp(-\text{Ri}_g^{-1})]$, for $r_0 = 2 \times 10^{-3}$ and $r_{\max} = 8$.

The primary difference between results from constant and variable r is that in the case of $r = r(\text{Ri}_g)$, the overflow core undergoes less dilution than with constant r. As less dilution better corresponds to the observations, results from this case are presented in the following section. We emphasize that the use of variable $r = r(\text{Ri}_g)$ alone does not guarantee good agreement with observations, as the modeled boundary layer structure and stratification must already be close to observed distribution for a Ri_g-dependent closure to lead to an improvement over the constant-r case.

5. Results

The results are organized as follows. First, the initial propagation of the density front is described. Second, results from a model–data intercomparison in the equilibrium phase of the simulation are presented. Third, entrainment rates are estimated from the model results in order to quantify turbulent mixing in the overflow plume.

TABLE 1. Parameters of the numerical simulation.

Basin size (x,z)	102 km × 941 m
Grid spacing (x,z)	$\Delta x = 73$ m, $\Delta z = 9$ m
Time step	$\Delta t \approx 1$ s, varies with CFL criterion
Rayleigh No.	Ra = 3000
Prandtl No.	$\mathrm{Pr}_T = \mathrm{Pr}_S = 10$
Density ratio	$R_\rho = 0.65$
Diffusivity ratio	$0.2 \times 10^{-2} \leq r\,(\mathrm{Ri}_g) \leq 1.6 \times 10^{-2}$
Horizontal diffusivities	$\nu_x = 5\ \mathrm{m^2\ s^{-1}}$, $K_{Tx} = K_{Sx} = 0.5\ \mathrm{m^2\ s^{-1}}$
Vertical diffusivities	$\nu_z = 1\text{–}8 \times 10^{-2}\ \mathrm{m^2\ s^{-1}}$, $K_{Tz} = K_{Sz} = 1\text{–}8 \times 10^{-3}\ \mathrm{m^2\ s^{-1}}$
Net transport	$\psi_{\mathrm{net}} = 105\ \mathrm{m^2\ s^{-1}}$
Relaxation coefficients	$\kappa_{\mathrm{in}} = 43\,200^{-1}\ \mathrm{s^{-1}}$, $\kappa_{\mathrm{out}} = 15\,300^{-1}\ \mathrm{s^{-1}}$

a. Description of the transient phase

The model is initialized with salinity and temperature profiles of Station 35 from REDSOX-1 observations, which are applied in the inlet relaxation zone (Figs. 4a, 5a). REDSOX-1 observations reveal the presence of a surface mixed layer, approximately 100 m thick, which is salty and warm because of heating and evaporation, and stably stratified [density ratio of the surface mixed layer $(2.4 \times 10^{-4}\ ^\circ\mathrm{C}^{-1} \times 11\ ^\circ\mathrm{C})/(9 \times 10^{-4}\ \mathrm{psu}^{-1} \times 0.4\ \mathrm{psu}) > 1$]. The incorporation of the surface mixed layer is important, since it occupies a significant portion of the water depth in most of the model domain, particularly near the inlet. As this layer has nearly constant properties along the channel, it is used as part of the initialization of the model fields (Figs. 4a, 5a).

The initial development of the system is that of the so-called lock-exchange flow (e.g., Keulegan 1958; Simpson 1987) in which the lighter fluid remains on top and the denser overflow propagates downslope. The overflow becomes turbulent, which is characterized by intense mixing and thickening of the plume by entrainment of ambient fluid (Figs. 4b, 5b; $t = 15$ h ≈ 0.6 days). The leading edge of the overflow exhibits a characteristic ''head.'' The head is one-half of a dipolar vortex, which is a generic flow pattern that tends to form in two-dimensional systems via the self-organization of the flow (e.g., Flierl et al. 1981; Nielsen and Rasmussen 1996) and which corresponds to the most probable equilibrium state maximizing entropy (Smith 1991). In three dimensions, this feature is observed as ''caps'' on top of vertical plumes (Turner 1962). A comprehensive investigation of the dynamics of the head in two-dimensional simulations of bottom gravity currents in comparison to that from laboratory experiments has been conducted by Özgökmen and Chassignet (2002). The head is a feature of the startup phase, and one would anticipate formation of this feature in the Red Sea when the overflow transport increases at the end of summer. The signature of the head is also pronounced in the surface mixed layer in the numerical simulation. However, no such oceanic observations exist to our knowledge, either because it is a very short-lasting process to capture or because the overflow transport increases gradually rather than abruptly. The overflow travels over complex topography and the leading edge of the overflow reaches the exit boundary at $t = 34$ h ($\approx$1.4 days) (Figs. 4c, 5c). The density signature of the overflow is quite diluted at this stage, with the bottom layer reaching only $S \approx 36.5$ psu and $T \approx 17\ ^\circ$C in the bowl between Stations 81 and 38, or approximately 3 psu and 8.5°C less than those at the top of the slope. Vigorous mixing takes place due to the small density difference from the ambient fluid. Further integration shows that higher salinity and temperature signals at the top of the slope propagate gradually downslope, with values in the bowl increasing to $S \approx 38$ psu and $T \approx 21.5$°C at $t = 90.9$ h ($\approx$3.8 days) (Figs. 4d, 5d).

The model is integrated until the salinity and temperature distributions in the system reach an equilibrium state, sample snapshots of which are shown in Figs. 4e, 5e (at $t = 189.4$ h ≈ 7.8 days). The overflow in the equilibrium state is characterized by a layer at the bottom 50–150 m thick, which is well mixed and transports the highest salinity and temperature signals along the channel with little dilution. Overlying is a layer of approximately equal thickness (100–200 m) in which T and S values get gradually diluted away from the bottom due to mixing with ambient water masses. Ambient water masses with low T and S values are sandwiched between the overflow and the surface mixed layer. Animations of the model output show that the overflow exhibits various waves, such as roll waves (i.e., a sequence of periodic hydraulic jumps propagating down the slope) that initiate from the plateau at Station 36. Breaking of internal waves intensifies following the steepening of the slope after Station 37, leading to enhanced entrainment. Localized mixing takes place at the sharp change in topography between Stations 83 and 81. Laminar wavetrains characterize the flow in the bowl between Stations 81 and 84.

The transient behavior of the system is also illustrated by plotting salinity at the bottom of Station 36 (near the top of the slope) and in the bowl between Stations 81 and 38 (near the bottom of the slope) as a function of time in Fig. 6a. This figure shows that it takes a longer time for the salinity to reach an equilibrium in the bowl than that at Station 36. This is not only because of the time offset in the arrival of the initial density front, but also because the speed of advection of high salinity (and temperature) water masses is small as they

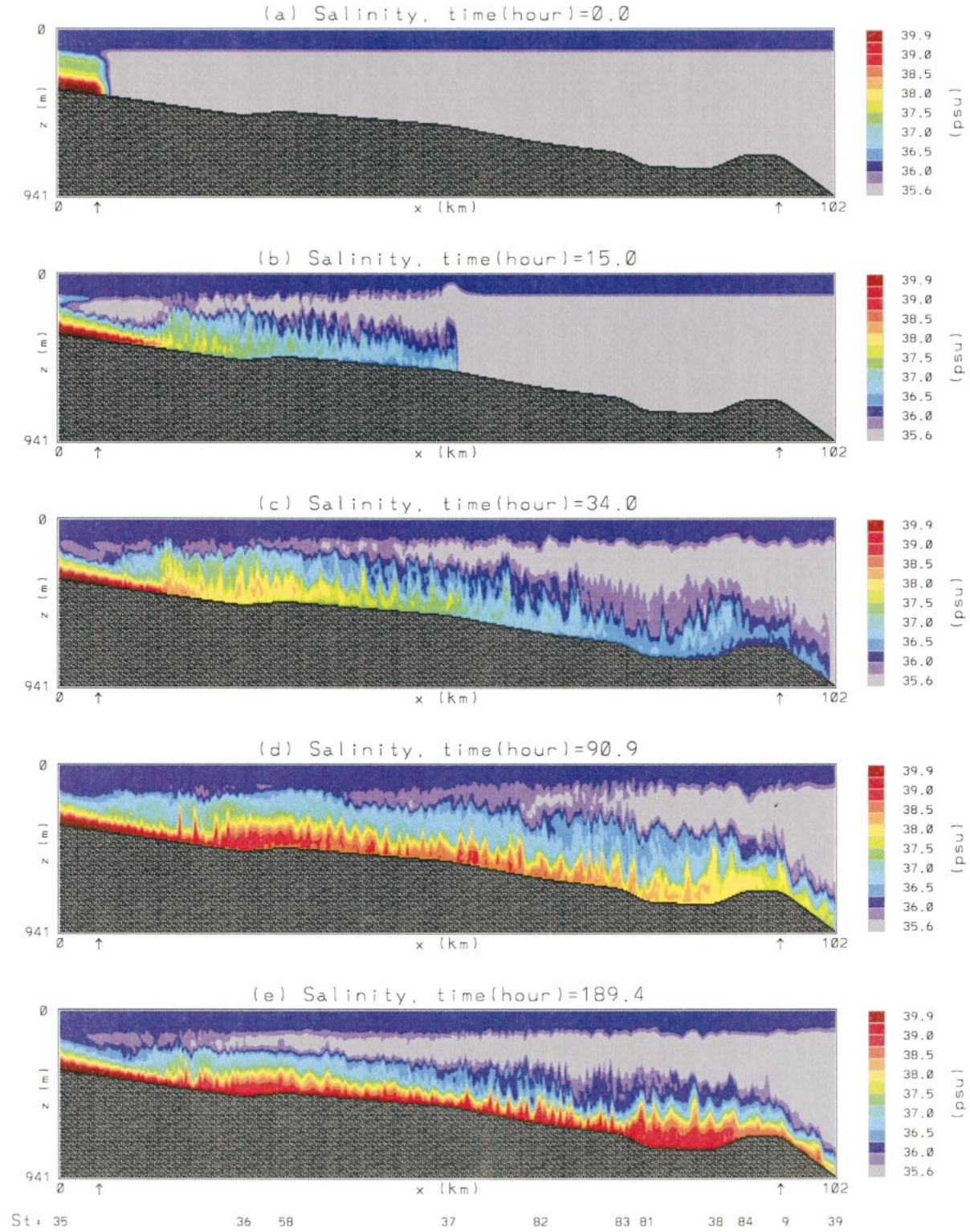

FIG. 4. Evolution of modeled salinity field as a function of time. Salinity distribution at (a) $t = 0$, (b) $t = 15$ h, (c) $t = 34.0$ h, (d) $t = 90.9$ h, and (e) $t = 189.4$ h. Survey station numbers and the extent of the buffer zones are marked.

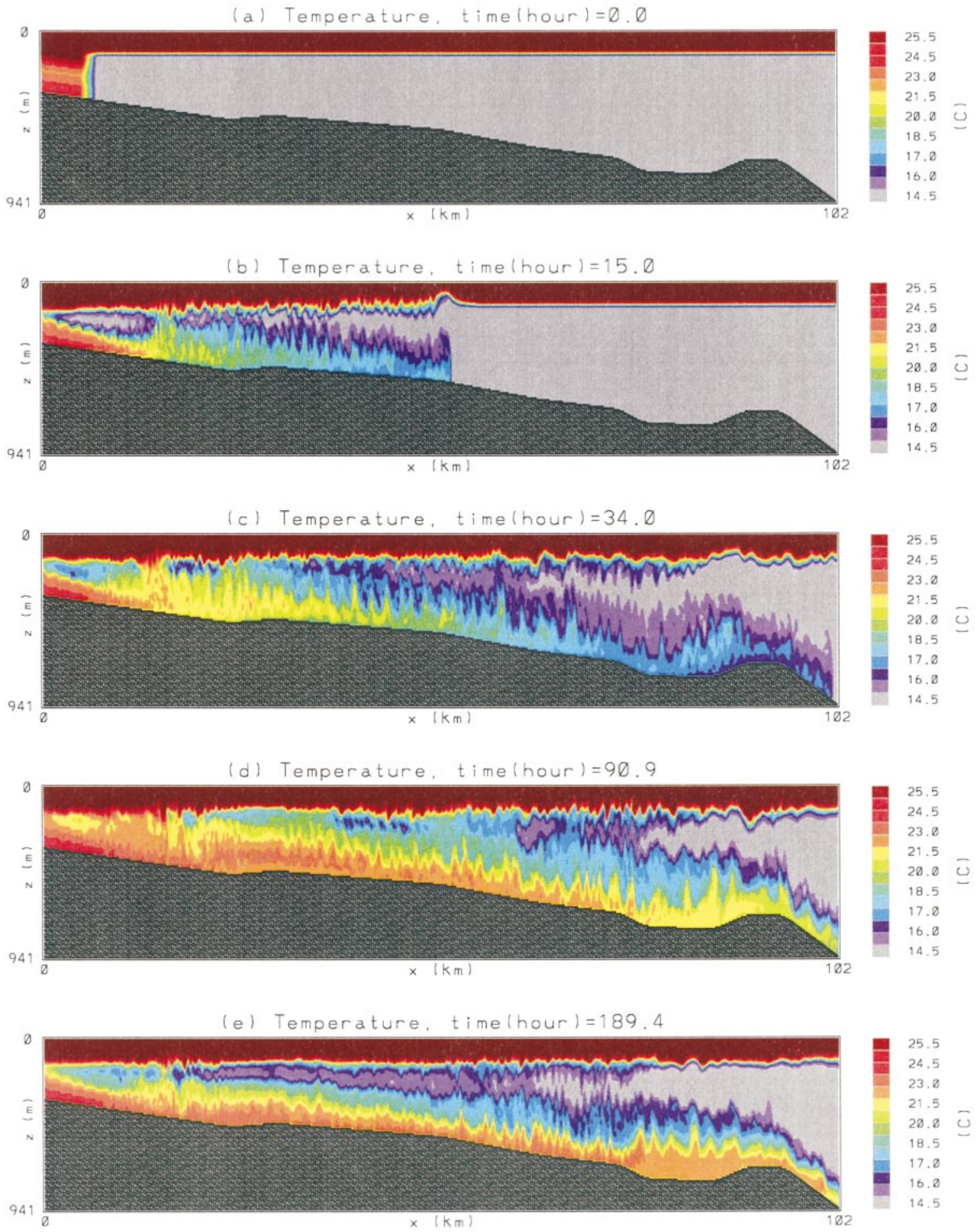

FIG. 5. Evolution of modeled temperature field as a function of time. Temperature distribution at (a) $t = 0$, (b) $t = 15$ h, (c) $t = 34.0$ h, (d) $t = 90.9$ h, and (e) $t = 189.4$ h.

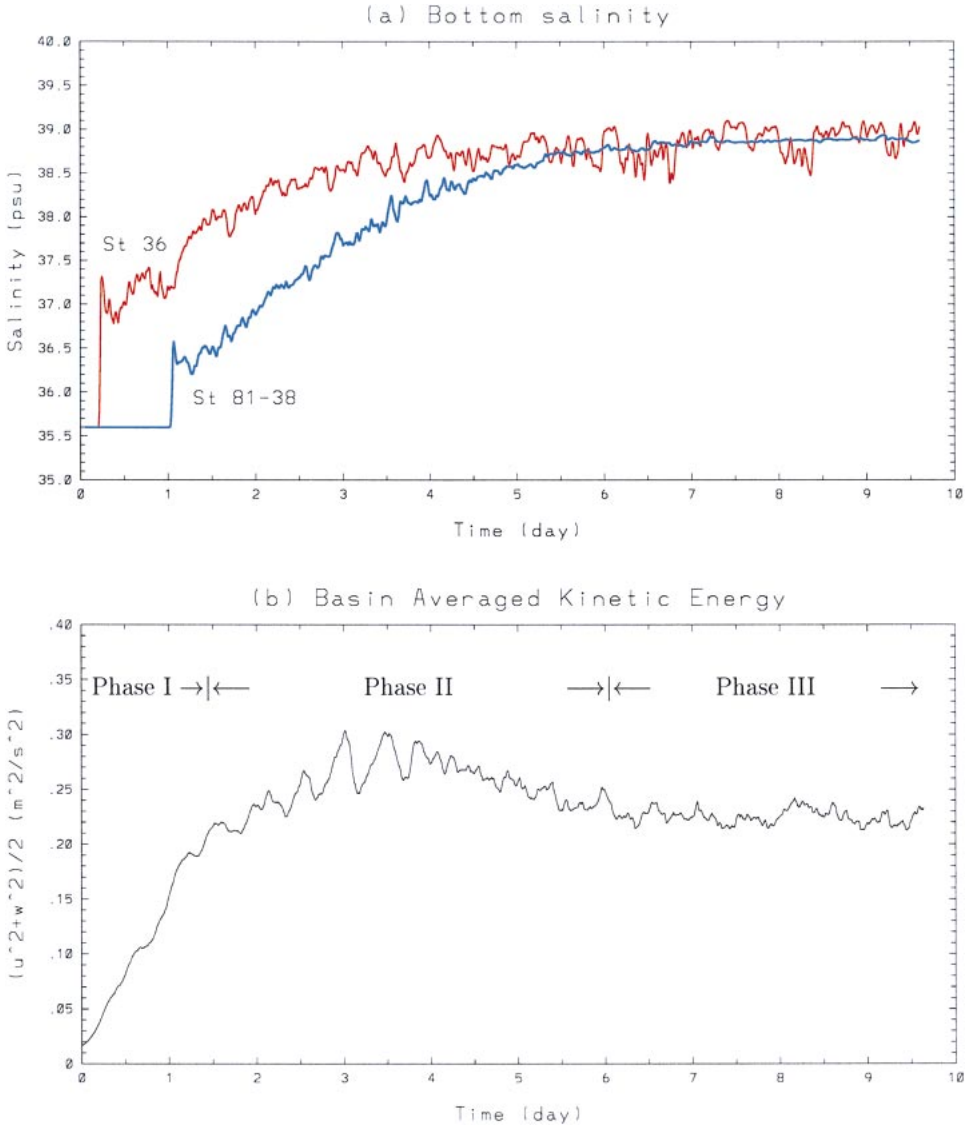

FIG. 6. (a) Salinity at the bottom of Station 36 (red curve) and between Stations 81 and 38 (blue curve), and (b) basin-averaged kinetic energy, KE = $\overline{|\nabla\psi|^2}/2$ ($m^2\ s^{-2}$), as a function of simulation period (days).

remain near the no-slip bottom. Salinities at both locations reach approximately the same equilibrium value; however, salinity at the bottom of Station 36 shows high variability, indicating that the waves (roll waves, internal waves and interaction with the surface mixed layer) cause mixing, while salinity in the bowl is nearly constant due to laminar wavetrains and small velocities at the bottom of the bowl. (Similar considerations apply to temperature as well; not shown.) Finally, the basin-averaged kinetic energy, KE = $\langle |\nabla\psi|^2/2\rangle$, is plotted as a function of time (Fig. 6b). The kinetic energy increases steadily while the density front crosses the domain in the first 1.4 days (Phase I). This is followed by a phase lasting 4–5 days, during which water mass characteristics in the system settle (Phase II). Note the peak of Phase II coincides with $t \approx 3.5$ days, at which salinity at the bottom of Station 36 reaches an equilibrium (in Fig. 6a), and then the entire system gradually slides to an equilibrium at $t \approx 6$ days (Phase III). The integration is terminated at $t \approx 10$ days.

b. *Equilibrium phase and model–data intercomparison*

One of the primary objectives of this study is to explore how well the model, which is subject to various simplifications in the equations of motion and parameters, as discussed above, can approximate REDSOX-1 observations of the outflow in the northern channel. In order to address this question, average salinity and temperature fields are calculated as usual, $\overline{S} = \tau^{-1} \int_{t_0}^{t_0+\tau} S\, dt$, where t_0 is a point in time during the equilibrium

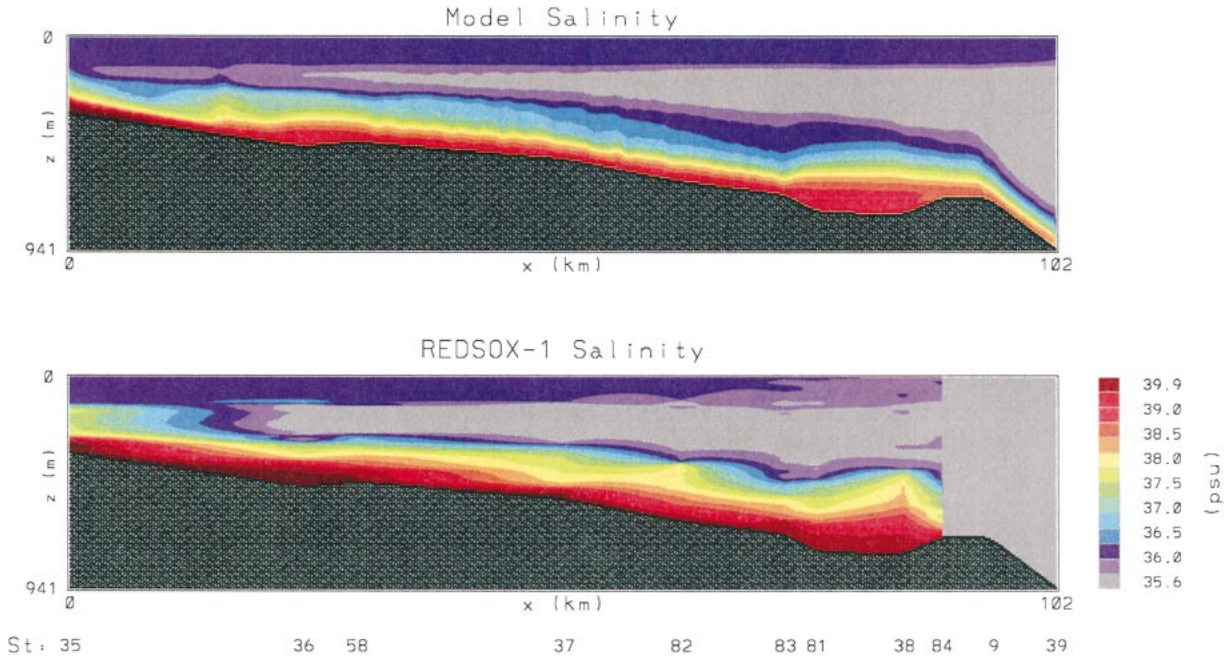

FIG. 7. Comparison of salinity distributions from (top) the model and (bottom) REDSOX-1 observations.

state (i.e., $t_0 \geq 6$ days) and the averaging period τ is large compared to the period of turbulent fluctuations such that $\overline{S'} \simeq 0$. An inspection of Fig. 6a indicates that $\tau > 1$ day and the mean quantities are calculated in the interval 6 days $\leq t \leq 9$ days.

Comparisons of salinity and temperature distributions from time-averaged model fields and from REDSOX-1 observations are illustrated in Figs. 7 and 8. REDSOX-1 temperature and salinity fields are plotted by interpolating between the stations. Observed fields are not shown at Stations 9 and 39 since this region coincides with model radiation zone, and the model fields do not reflect the underlying physics in this regime. Figures 7 and 8 indicate that the model and observations show good agreement on the general characteristics of the system: (i) the gradual thickening of the overflow with downslope distance, with pronounced increase in thickness in the bowl between Station 81 and 38; (ii) the advection of high salinity and temperature signals at the bottom layer throughout the channel with little dilution; and (iii) ambient water masses sandwiched between the overflow and surface mixed layer.

A quantitative comparison is carried out by plotting model-mean salinity and temperature fields and REDSOX-1 observations for the first nine stations within the model domain (Figs. 9 and 10). The variability range of the model profiles during the equilibrium state is shown by the dashed curves in Figs. 9 and 10. Figure 9 indicates that at the inlet (Station 35), the relaxation procedure allows for the model to deviate somewhat from the observed profile just below the surface mixed layer, which appears to be diluted by advection of ambient water masses. The model salinity in the bottom layer is reduced rather significantly by the next station (Station 36), more so in the model than in observations, and this deficiency is maintained at the same level at all other stations. There are also other deviations of the model fields from the observations, that are particularly visible at Station 37, at which the overflow layer is thicker in the observations than that in the model. However, the REDSOX-1 profiles are generally within the range of the model mean and variability. Similar results are obtained for temperature profiles (Fig. 10). Overall, the agreement between the model and observations appears satisfactory.

The difference between the model and REDSOX-1 salinity and temperature fields is quantified using

$$S^i_{\text{error}} \equiv \frac{\sqrt{\frac{1}{N^i}\sum_{j=1}^{j=N^i}[\overline{S}^i_{\text{model}}(j) - S^i_{\text{obs}}(j)]^2}}{\Delta S},$$

$$T^i_{\text{error}} \equiv \frac{\sqrt{\frac{1}{N^i}\sum_{j=1}^{j=N^i}[\overline{T}^i_{\text{model}}(j) - T^i_{\text{obs}}(j)]^2}}{\Delta T}, \qquad (6)$$

where $\overline{S}^i_{\text{model}}$ ($\overline{T}^i_{\text{model}}$) is time-averaged model output, and S^i_{obs} (T^i_{obs}) is REDSOX-1 values at station i, N^i is the number of sampling points at station i, and S^i_{error} (T^i_{error}) is the rms error normalized by salinity range $\Delta S = 4.3$ psu ($\Delta T = 11$ °C) in the system. It is worth pointing out that the observations are nonsynchronous instantaneous measurements, whereas the model quantities are time averaged. Here $\overline{S}_{\text{error}}$ and $\overline{T}_{\text{error}}$ are plotted as a function of distance (station) in Fig. 11, which shows that

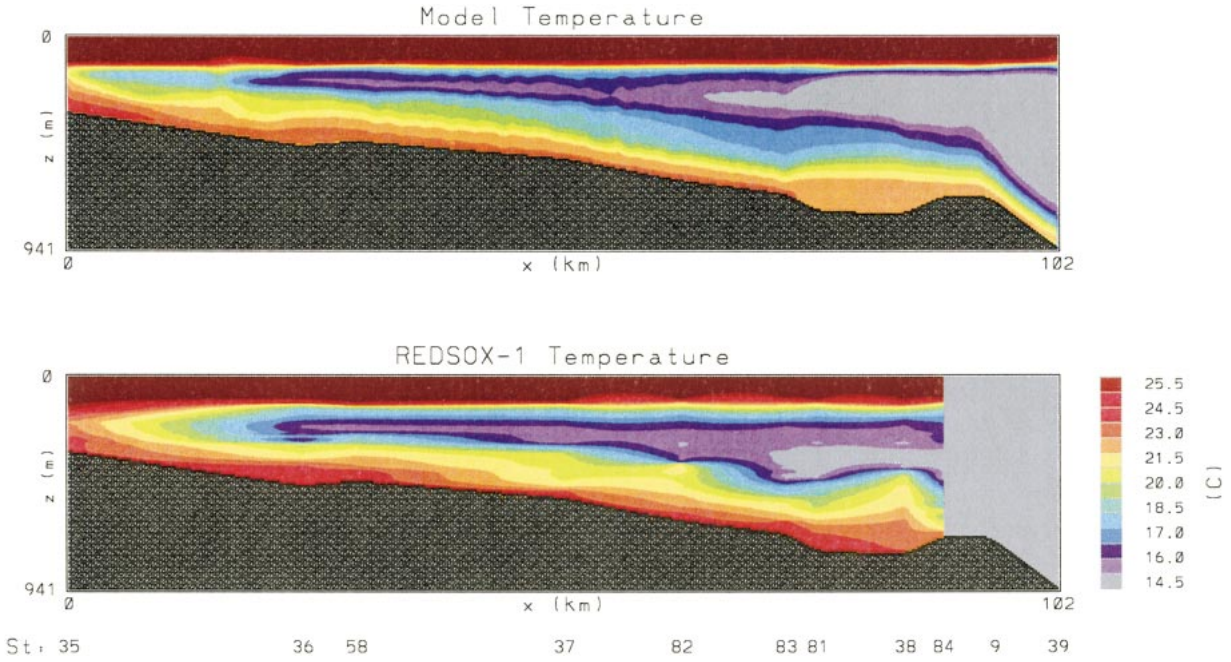

FIG. 8. Same as Fig. 7 but for temperature.

these quantities are in the range of 6%–16%. The main result from this figure is that the errors are approximately uniform for both salinity and temperature, and in distance, which appears to be indicative of model consistency.

As the error metric (6) includes not only the overflow plume, but also the ambient water masses and the surface mixed layer, it does not quantify accurately the errors of the simulated plume, which are particularly pronounced near the bottom. Therefore, the model deficiencies are better highlighted by a direct comparison of bottom salinity and temperature from the model and observations. Figure 12a illustrates the very small and gradual decrease in the bottom salinity from observations. In contrast, the bottom salinity from the model simulation decreases significantly only at Station 36 and 58, and then remains constant until near the exit. This initial dilution of the bottom salinity is considerably larger than the observed dilution. This behavior is found to be insensitive to model parameters. One possible explanation of this disagreement is that Station 35, which is used to initialize and force the plume may be unrepresentative of the average conditions during the period of the observational survey of the plume due to effects of time dependence and three-dimensionality. In particular, it is found that any errors arising from sampling the high salinity layer at the bottom of Station 35 (Fig. 9) may play an important role in the simulation. The outflow near the strait is subject to large tidal modulation, which could cause the salinity and temperature profiles at Station 35 to be atypical; the high salinity outflow layer in fact appears abnormally thin at this station. To explore this hypothesis, the depth of the high salinity and high temperature layer at the inlet is artificially (and arbitrarily) increased by 20 m (2 grid points) by modifying the topographical and observational data. While modification of the slope angle is negligibly small ($\Delta\theta = 0.04^\circ$), a 20-m increase in the overflow layer depth corresponds to about 20% increase of the mass of this layer at the inlet. The results from this experiment exhibit a partial correction in the bottom salinity in the model (Fig. 12a), while the changes in the rest of the profiles (not shown) are small. The modification of bottom temperature is small (Fig. 12b), but note that observed bottom temperature increases slightly at Station 36, indicating deviations from statistical mean state or two-dimensionality. We conclude that the deviation of bottom salinity and temperature in the model from observations may be related in part to observational profile of the overflow plume at the inlet to the domain, which could include sampling errors, or effects of time dependence and three-dimensionality.

c. *Entrainment*

Definition of entrainment is highly problem dependent (e.g., Meleshko and van Heijst 1995) and no unambiguous, general definition of entrainment exists that applies equally well for all mixing problems. For bottom gravity currents, an additional complication has been that they have been thus far investigated mostly during the startup phase because of complications in the laboratory setup to attain an equilibrium. However, the entrainment characteristics during the transient phase are thought to differ from those during the equilibrium for overflows (Beckmann 1998; J. Price 2001, personal

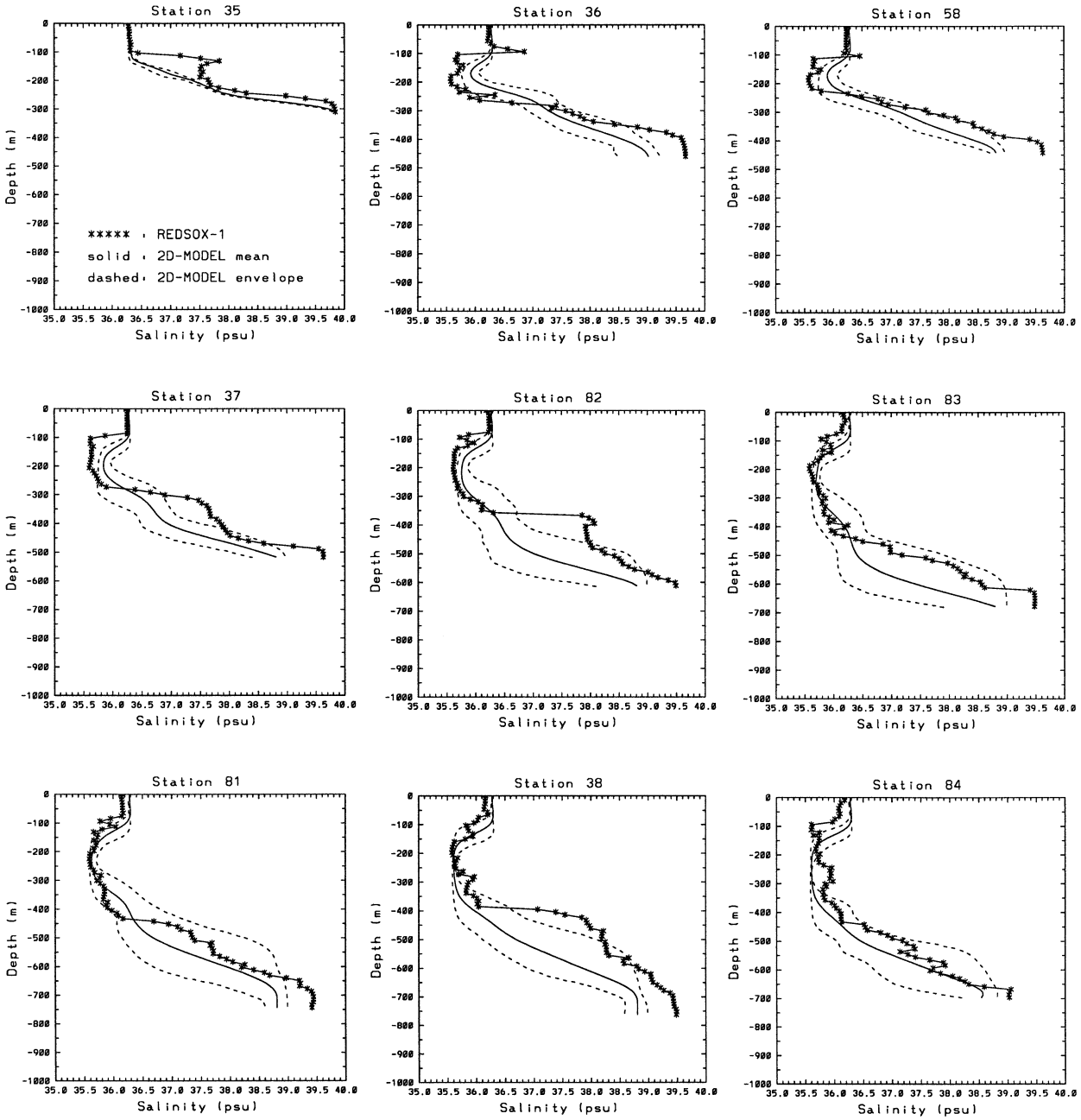

FIG. 9. Comparison of salinity profiles from REDSOX-1 observations and the model. Salinity is plotted as a function of water depth (m) at each REDSOX-1 station within the model domain (curves marked with asterisks). Solid curves show time-averaged model profiles and dashed curves mark the range of variability of the profiles in the model simulation during equilibrium state.

communication). Therefore, various entrainment metrics, which have been developed specifically to quantify entrainment during startup phase (e.g., Hallworth et al. 1996; Özgökmen and Chassignet 2002) are not the optimal choice for oceanic overflows.

Here, we quantify entrainment in the equilibrium state using the definition of Morton et al. (1956),

$$E \equiv \frac{w_E}{U}, \tag{7}$$

where E is the entrainment parameter defined as the ratio of net entrainment velocity w_E and the local current speed U. For two-dimensional gravity currents over small slopes,

$$E \approx \frac{(\Delta Q/l)}{(Q/h)}, \tag{8}$$

where Q is the overflow transport, h is the overflow thickness, and ΔQ is the change in overflow transport over a distance l along the slope.

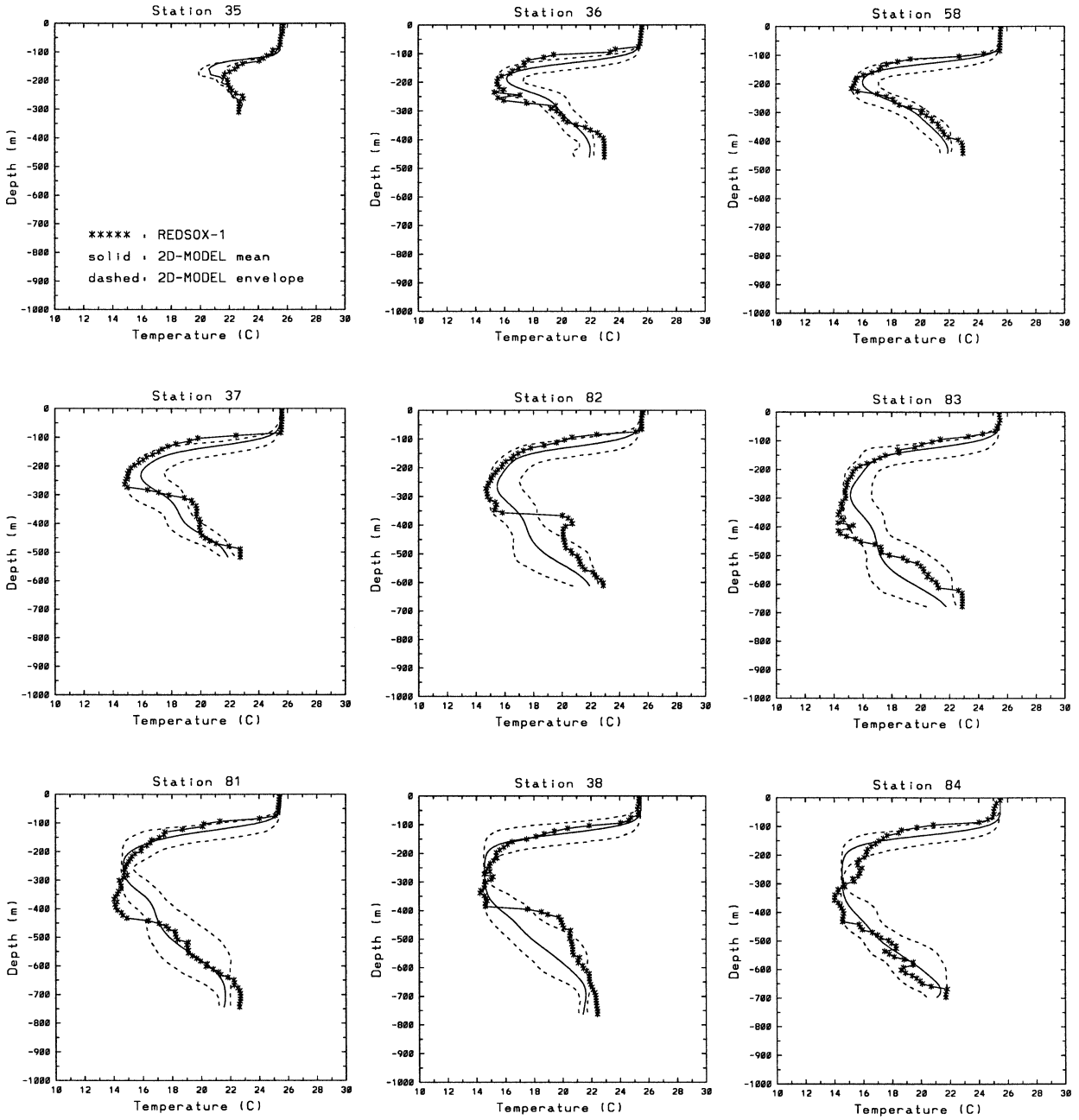

FIG. 10. Comparison of temperature profiles from REDSOX-1 observations and the model. Refer to caption of Fig. 9 for other details.

In order to visualize the nature of mixing and entrainment qualitatively, approximately 1000 Lagrangian particles are released into the flow field during the equilibrium state (at $t \approx 8$ days) and are advected for 1 hour. The trajectories shown in Fig. 13 (see figure caption for further details) indicate that following a nearly laminar regime near the channel inlet, the overflow exhibits strong vertical mixing just before reaching the plateau at Station 36. Strong dilution of the bottom overflow layer takes place most likely due to shallow water depth and strong shear. Also the relatively thin bottom layer allows the mixing on the interface penetrate through the whole layer. Between Stations 36 and 58, the flow becomes regular again until the slope angle increases after passing Station 37. Between Stations 37 and 81, there appears to be vigorous interaction between the ambient fluid and the upper layer of the overflow. This complex interaction can be approximately characterized partly as internal wave motion and partly as ambient fluid being engulfed by the coherent structures of the overflow, with entrainment being confined to the upper layer of the overflow. Note that particles appear to be strongly con-

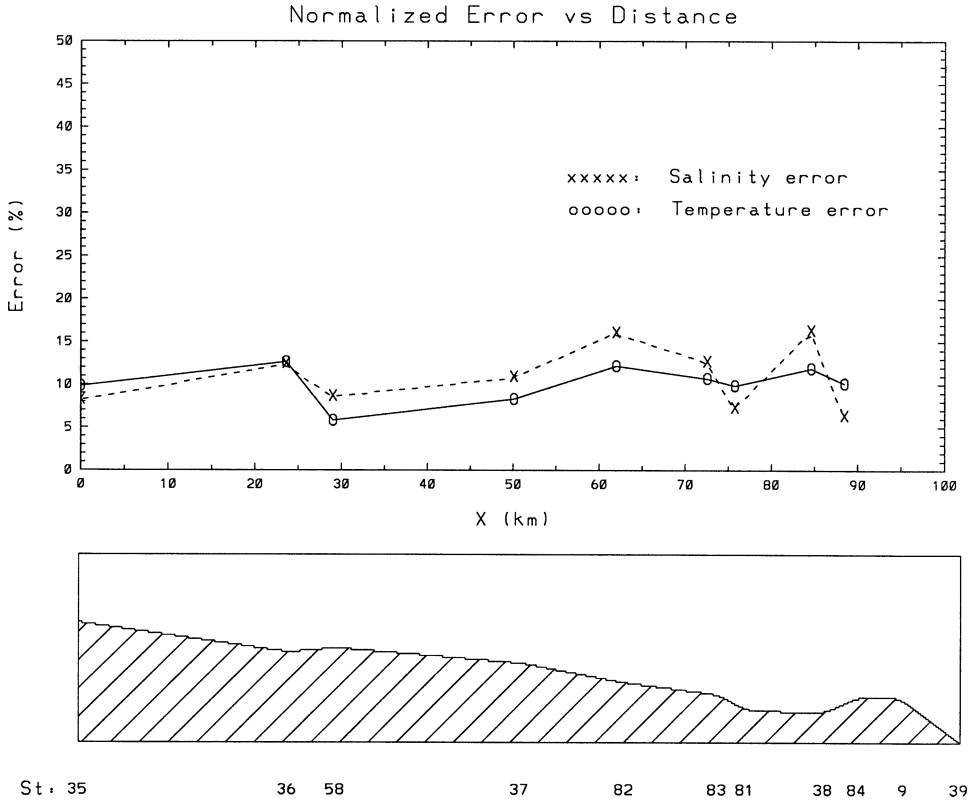

FIG. 11. Normalized salinity and temperature errors, S_{error} and T_{error} (%), between model and REDSOX-1 observations as a function of distance in the domain (km). The topography and station numbers are shown in the lower panel.

strained to follow the interface between the bottom overflow layer ($S \geq 38$ psu) and the upper overflow layer. Therefore, there is little mixing across this interface in the downstream regions of the plume, which explains why the bottom salinity and temperature remain almost unchanged after Station 58. Another interesting feature is the counter flow of the ambient water below the mixed layer (see also Figs. 14a,b).

In order to estimate entrainment quantitatively, the mean transport streamfunction $\overline{\psi}$ is calculated during the equilibrium phase $6 \leq t \leq 9$ days. Figure 14b illustrates the gradual entrainment of ambient water into the outflow along the slope and the subsequent generation of a middepth jet, which flows in the opposite direction to the overflow below the nearly quiescent surface mixed layer. The increase in transport is quantified by plotting the quantity $[Q(x) - Q^{in}]/Q^{in}$, where $Q(x)$ is the transport of the overflow as a function of downslope distance x and Q^{in} is the overflow transport at the inlet, Station 35. Figure 14c clearly illustrates that the transport increase in the northern channel can be divided into distinct regimes, in which the transport changes approximately linearly. Linear increase in transport starts with Stations 35–36 (segment 1), continues at a reduced rate between Stations 58 and 37 (segment 2) when the slope angle reduces, increases significantly between Stations 37 and 83 (segment 3) when the slope angle increases again and shuts off in the plateau between Stations 81 and 38 (segment 4). The last section, segment 5 is influenced by radiation boundary conditions, and is not considered here. The peaks in the curve $[Q(x) - Q^{in}]/Q^{in}$ near Stations 36 and 83 are associated with localized circulation cells that appear to be induced by sharp changes in slope angle at these locations. The impact of these localized features can be neglected at first order. The general picture that emerges from Fig. 14 is that changes in the overflow transport are strongly correlated with changes in slope angle. The average angle $\overline{\theta}$ of each slope segment, transport increase ΔQ over a segment with length l, and their ratio $w_E = \Delta Q/l$ are tabulated in Table 2. Note that while both the outflow transport and thickness vary over each segment, their ratio $U = Q/h$ is approximately constant, and is shown in Table 2. Last, E is estimated from (8), and plotted as function of $\overline{\theta}$ in Fig. 15. A least squares approximation to data points yields

$$E \approx 3.5 \times 10^{-3}\overline{\theta}. \tag{9}$$

Entrainment parameter quantified by (9) needs to be

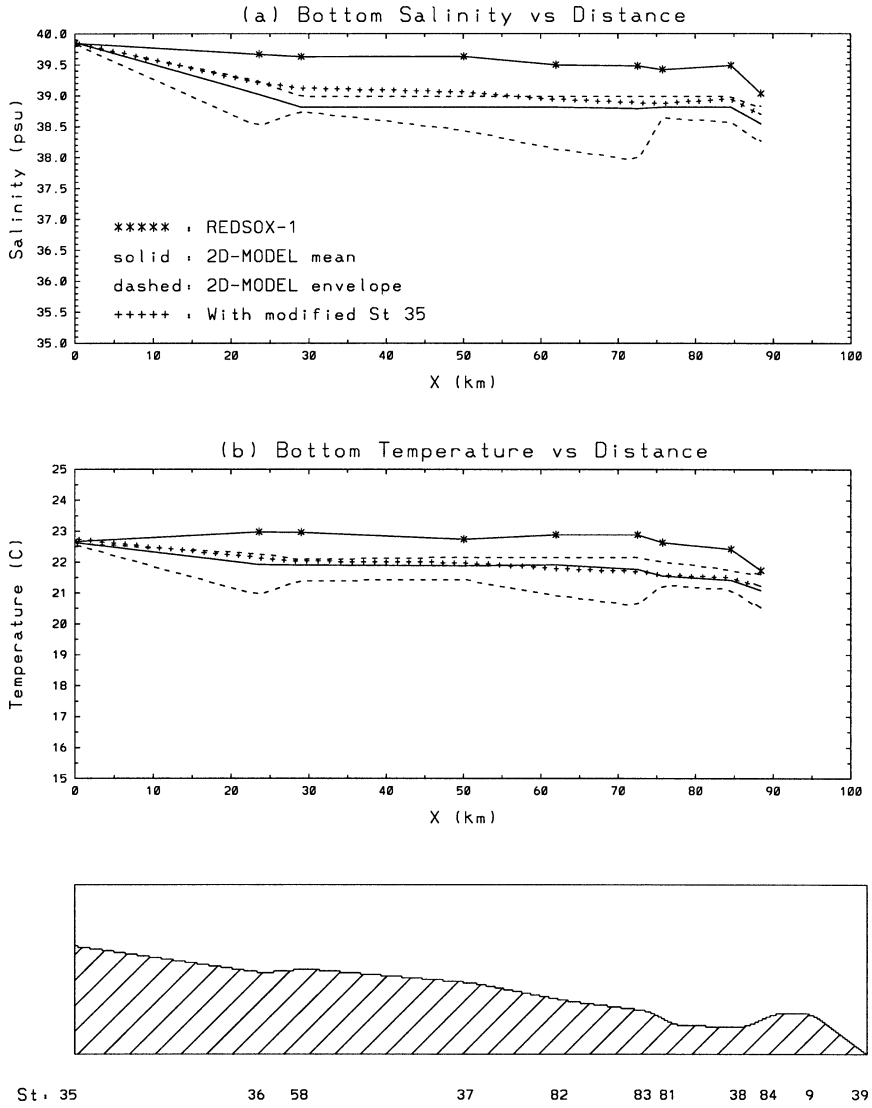

FIG. 12. Comparison of (a) bottom salinity and (b) bottom temperature from REDSOX-1 observations (curves marked with asterisks) and time-averaged model (mean: solid; dashed: envelope) as a function of distance in the domain (km). The curves with crosses depict the mean bottom salinity and temperature resulting from an experiment with modified inlet profiles at Station 35. The topography and station numbers are shown in the lower panel.

compared with others from laboratory and numerical experiments. Turner (1986) reports

$$E \approx 10^{-3}(5 + \theta), \tag{10}$$

which yields entrainment parameters that are 2.5–6 times larger than those estimated from (9). However, (10) is based on laboratory experiments with slopes of $9^\circ \leq \theta \leq 90^\circ$, whereas the average slope angle in the northern channel is about 0.3°. Özgökmen and Chassignet (2002) reported from numerical experiments

$$E \approx 5.6 \times 10^{-3}\theta, \tag{11}$$

for the startup phase of bottom gravity currents over slopes with $1^\circ \leq \theta \leq 5^\circ$. This is not quite a factor of 2 larger than (9), which is more consistent with stronger mixing in the startup phase than in the equilibrium phase of a plume.

The entrainment parameter E is expressed also as a function of the bulk Richardson (or Froude) number based on the ratio of internal wave speed and local flow speed (e.g., Turner 1986; Baringer and Price 1997b)

$$\mathrm{Ri}_0(x) \equiv \frac{g[\beta\delta S(x) - \alpha\delta T(x)]h(x)}{\delta U(x)^2}, \tag{12}$$

where h is the local overflow layer thickness, $\delta S = S_o - S_a$, $\delta T = T_o - T_a$, and $\delta U = U - U_a$ are the salinity, temperature, and speed differences between the overflow and ambient layers. The bulk Richardson number

is estimated both from the model simulation and REDSOX-1 measurements. As the model fields are time averaged, continuous, and smooth, the overflow layer is defined simply to extend from the bottom to the point at which the velocity changes sign (counterflow: Figs. 14a,b). The thickness of the ambient water layer is measured from the base of the surface mixed layer.

The overflow speed $U(x)$ for both the equilibrium state of the numerical simulation and REDSOX-1 data are shown in Fig. 16a [the superimposed flat lines indicate the discrete average values for slope segments 1–4 used in estimation of the relationship (9)]. There is a reasonable agreement between estimates from the model and data, in particular regarding the acceleration and deceleration of the overflow along various slope segments. The entrainment velocity w_E and the entrainment parameter E estimated from the model are illustrated in Figs. 16b,c. A comparison of the bulk Richardson number Ri_0 estimates from the model and data indicate that Ri_0 is typically underestimated in the model (Fig. 16d). This result is to be expected as the shear δU^2 is slightly higher in the model due to somewhat higher overflow and counterflow speeds, and also the stratification is weaker due to larger dilution of model temperature and salinity in the bottom layer (Figs. 7–10). Slightly weaker stratification and stronger shear yield lower Ri_0 in the model than that from REDSOX-1 data. However, the difference is reasonably small (rms difference is approximately 40%), and the overall pattern is reproduced. Note the lower Ri_0 along slope segments 2–3 and high Ri_0 along segment 4 to coincide with high entrainment and negligible net entrainment regimes, respectively. It is clear from Figs. 16c,d that, as the Ri_0 decreases (increases), E increases (decreases).

The relationship between Ri_0 and E is investigated using a scatter plot of Froude number ($\mathrm{Fr} = \sqrt{\mathrm{Ri}_0^{-1}}$) and entrainment parameter. Figure 17 illustrates these curves for slope segments 1–4. Clearly, a close relationship exists, but it has a complex form. Instead of trying to fit empirical curves, we explore how this scatter plot relates to existing results. Ellison and Turner (1959) estimated this relationship based on laboratory results at high slope angles

$$E = \frac{0.08 - 0.1\mathrm{Ri}_0}{1 + 5\mathrm{Ri}_0}. \tag{13}$$

However, (13) yields implicitly no entrainment for $\mathrm{Ri}_0 > 0.8$, which is the case throughout most of the model domain (Fig. 16d). An equivalent approximate expression that covers the range of $\mathrm{Ri}_0 > 0.1$ is (Lofquist 1960; Turner 1973; Fernando 1991; Baines 2001)

$$E \approx \frac{0.001}{\mathrm{Ri}_0}, \tag{14}$$

which is in reasonable agreement with the scatter plot from model results in Fig. 17. We plot $E(\mathrm{Fr})$ from the Mediterranean outflow observations (mean values are

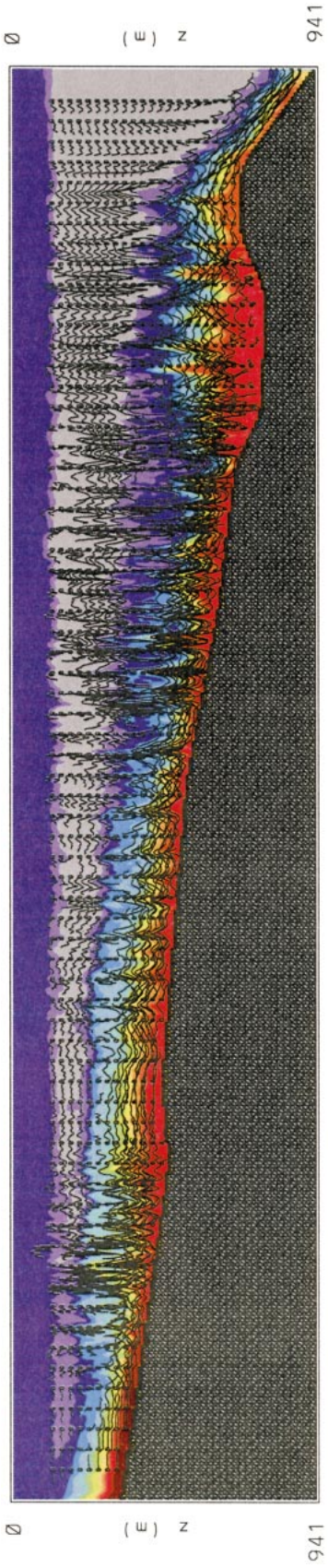

FIG. 13. Trajectories of approximately 1000 Lagrangian particles released into the flow field between $t = 189.5$ and 190.5 h in a regular array (with a horizontal spacing of approximately 1500 m or every 20 grid points and a vertical spacing of approximately 30 m or every 3 grid points). Salinity field is plotted in the background at $t = 190.0$ h (refer to Fig. 4 for the color bar).

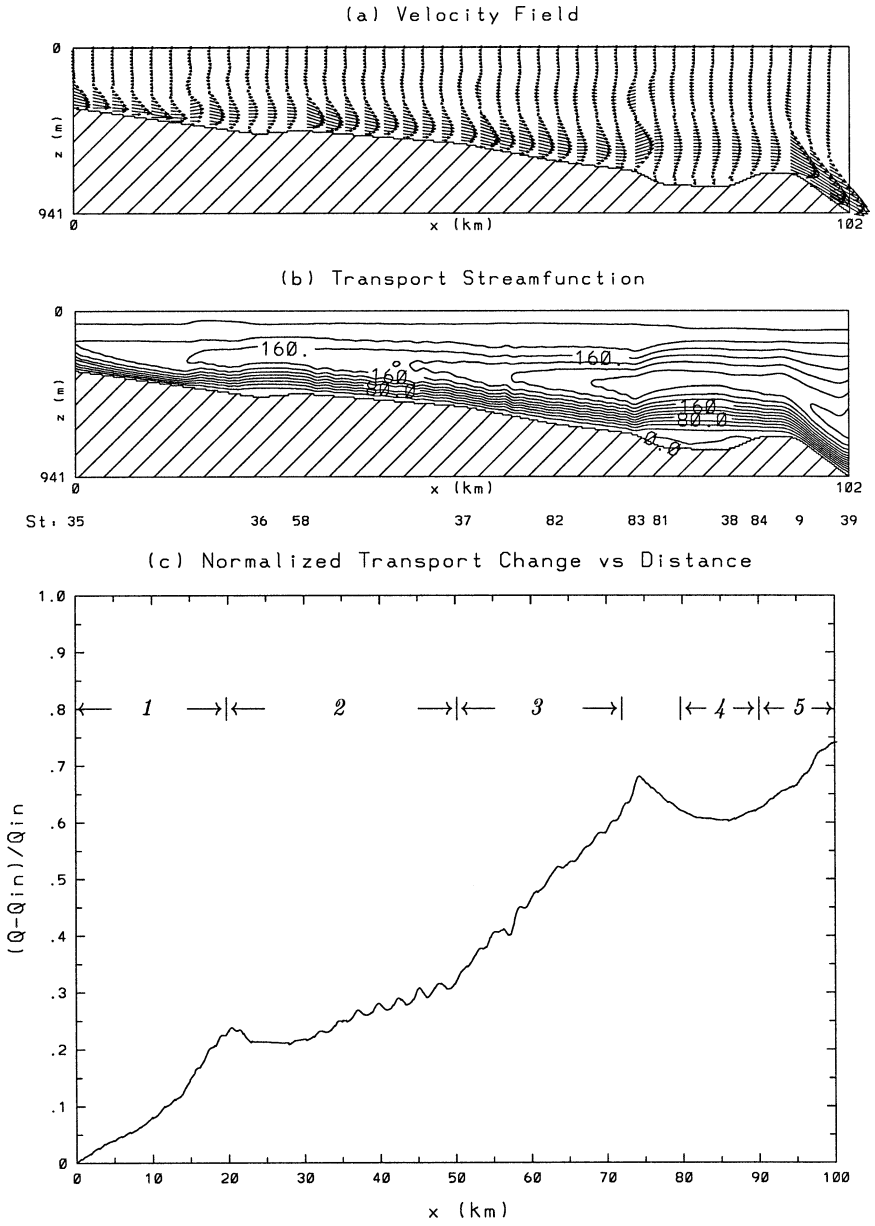

FIG. 14. (a) Time-averaged velocity field [vectors at every 35 (2) grid points in the horizontal (vertical) direction are shown; max vector scale is 2 m s^{-1}] and (b) transport streamfunction $\overline{\psi}$ (contour interval: 20 m^2 s^{-1}) in the equilibrium state; normalized change in overflow transport, $(Q - Q^{in})/Q^{in}$, as a function of distance in the channel (km) and slope segments 1–5 indicating that changes in the entrainment rate are correlated with changes in the slope angle.

TABLE 2. The net transport increase ΔQ over a slope segment with length l and average slope angle $\overline{\theta}$. Mean overflow speed U and entrainment velocity w_E are tabulated as a function of each segment, and entrainment parameter E is estimated.

Segment	$\overline{\theta}$ (°)	ΔQ (m^2 s^{-1})	l (m)	U (m s^{-1})	w_E (m s^{-1})	E
1, Stations 35–36	0.33	20	20×10^3	1.0	1×10^{-3}	1.0×10^{-3}
2, Stations 58–37	0.16	12	27×10^3	0.85	0.425×10^{-3}	0.5×10^{-3}
3, Stations 37–83	0.41	33	26×10^3	0.85	1.275×10^{-3}	1.5×10^{-3}
4, Stations 81–38	0.01	0	8×10^3	0.60	0	0

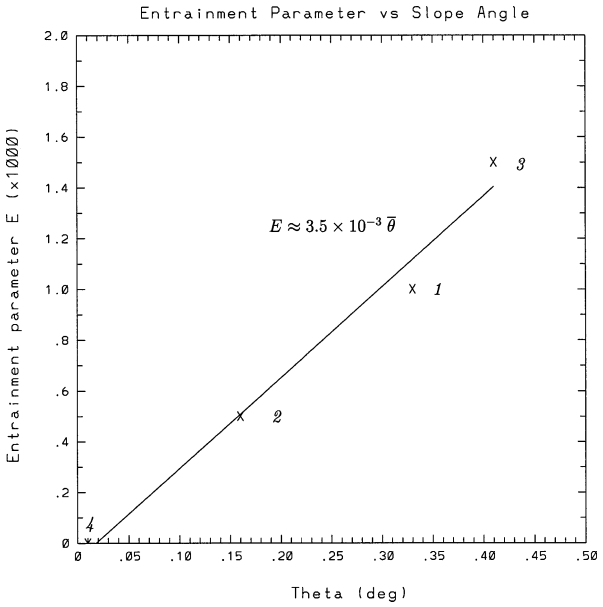

FIG. 15. Entrainment parameter E estimated at slope segments 1–4 is plotted as a function of slope angle $\overline{\theta}$ at each segment. The solid line shows the least squares fit to sampling points (marked by $\times$), $E \approx 3.5 \times 10^{-3}\,\overline{\theta}$.

plotted from Fig. 7b in Baringer and Price 1997b), which is also in the same range as the scatterplot from the model simulation. The main conclusion is that E is roughly inversely proportional to Ri_0 (or proportional to Fr). Alternative power laws to (14) are not investigated here, as they may not hold a more precise meaning when based on the narrow parameter range of the present study. Note also that from (9) and (14), one gets the empirical but intuitive relationship $\mathrm{Ri}_0^{-1} \sim \overline{\theta}$, which states the importance of the topographic slope angle (which is a parameter of the domain geometry and is usually known) in determining the main mixing parameter (which is a complex function of stratification and flow speeds, and is not known a priori).

It is instructive to further consider entrainment results with respect to those reported by Baringer and Price (1997b), as $\mathrm{Ri}_0 \approx 2.0$ (Fr = 0.7) for both the Mediterranean overflow at the exit from the Strait of Gibraltar, and the Red Sea outflow (winter) at northern channel entrance. Entrainment velocities w_E in the numerical simulation range from 0.425 mm s^{-1} along segment 2 to 1.275 mm s^{-1} along segment 3, leading to a transport increase of approximately 65% along the first 70 km in the northern channel (Fig. 14c). In comparison, Baringer and Price (1997b, their Fig. 7a) show, based on transport measurements, w_E in the range of 0.2–1.3 mm s^{-1}, and a transport increase of approximately 100% along the first 50 km of the Mediterranean overflow after exiting the Strait of Gibraltar. Therefore, the net entrainment velocity estimates appear to be in the same range between those calculated here from the Red Sea outflow model and those based on the Mediterranean overflow observations by Baringer and Price (1997b). The difference in transport increase is surmised to be due to three-dimensional effects, as the Mediterranean overflow widens from 12 to 30 km over this distance. As the entrainment velocity estimates are averaged over the width of the plume, one can normalize entrainment velocity estimates by multiplying by the ratio of current width and initial width. This calculation (using Table 1 and Fig. 7a from Baringer and Price 1997b) indicates that effective entrainment velocities in excess of 1.3 mm s^{-1} are sustained in the Mediterranean outflow over a distance of 30–35 km (or their sections A–D, specifically), whereas such high entrainment velocities are estimated here only in segment 3 (or St. 37–81) over a distance of 20–25 km. Equivalently, the entrainment parameter estimated for the Mediterranean outflow is in the range of $0.6 \times 10^{-3} \leq E \leq 1.9 \times 10^{-3}$, which is somewhat higher than that for the modeled Red Sea outflow in the northern channel (Fig. 17) and accounts for the ratio of 3/2 in transport increase in these two overflows. The difference in entrainment can be attributed at first order to higher slope angle along the path of the Mediterranean outflow (between Sections A and D), $\overline{\theta} \approx 0.6°$, whereas $\overline{\theta} \leq 0.4°$ in the northern channel, while the complex three-dimensional motion presumably also plays a role in the Mediterranean overflow.

Overall, the general range of the entrainment velocities, entrainment parameter, and its functional dependence on local bulk Richardson/Froude number estimated from the numerical simulation appears to be quite reasonable, with differences from previous estimates reflecting the special characteristics of the Red Sea outflow in the northern channel, namely the small slope angles and the laterally constrained flow by channel topography.

6. Summary and discussion

The present study is motivated by the fact that most deep and intermediate water masses are released into the large-scale ocean circulation from high latitude and marginal seas in form of overflows. It is known that not only is the strength of the thermohaline circulation sensitive to details of mixing of overflows with ambient water masses, but also that such processes pose significant numerical and dynamical challenges for ocean general circulation models (Price and Baringer 1994; Willebrand et al. 2001; Beckmann and Döscher 1997; Winton et al. 1998; Killworth and Edwards 1999; Nakano and Suginohara 2002). This paper reports on a model–data intercomparison study focused on a narrow channel on the path of the Red Sea overflow, which carries approximately two-thirds of the total overflow transport. The width of the channel is much smaller than the radius of deformation of the overflow, such that the overflow is strongly constrained in the lateral direction, which allows the effects of three-dimensional motion and rotation on the flow dynamics to be neglected at

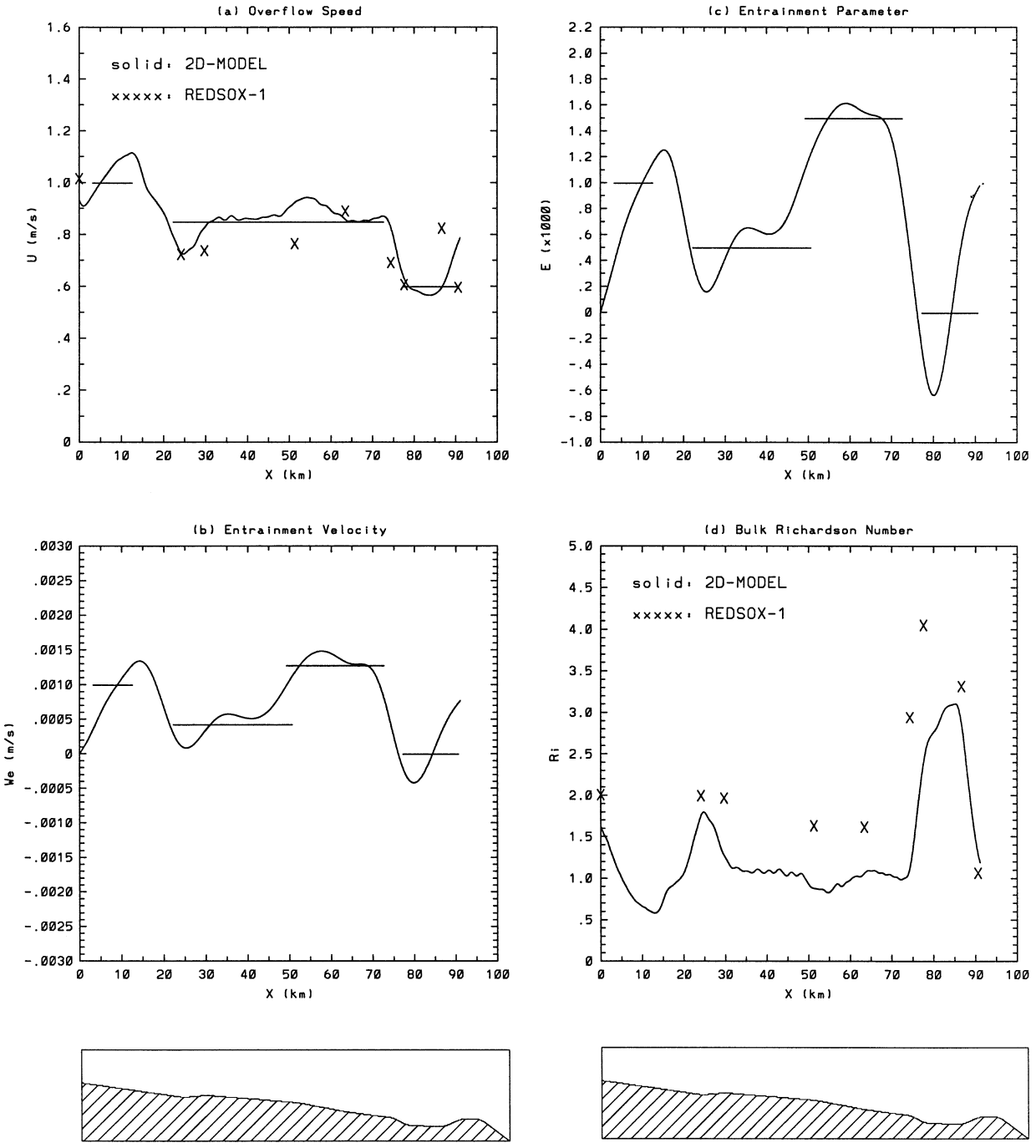

FIG. 16. (a) Overflow speed U (m s^{-1}), (b) entrainment velocity w_E (m s^{-1}), (c) entrainment parameter E, and (d) bulk Richardson number Ri_0 as a function of distance $\times$ (km). Continous solid lines indicate results from the model simulation, and estimates from REDSOX-1 station data are marked with $\times$. The flat lines indicate the average values listed in Table 2 for slope segments 1–4.

first order and a two-dimensional model to be used. The model is forced by temperature and salinity profiles from the recent REDSOX winter cruise (Bower et al. 2002; Johns et al. 2002; Peters et al. 2002) and radiation conditions at the exit end with the objective of simulating and approximating the interior dynamics. The novel aspects of this study are that it is the first investigation (to our knowledge) that which involves (i) numerical simulation of bottom gravity currents along complex topography until an equilibrium is reached (bottom gravity currents have been traditionally investigated in the laboratory and numerically during the start-up phase over slopes with constant angle) and (ii) direct intercomparison of data from an oceanic overflow and results

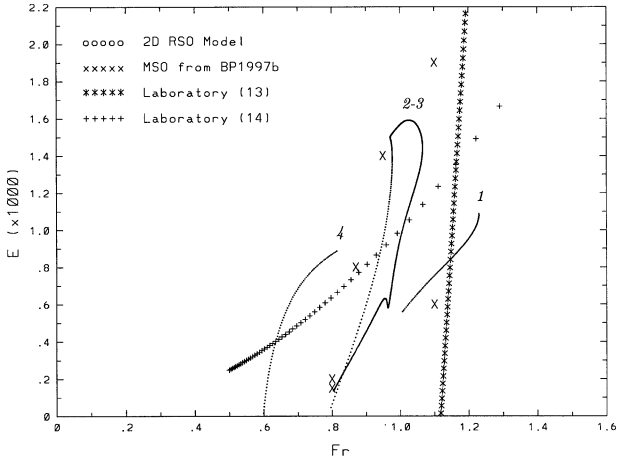

FIG. 17. Scatterplot of entrainment parameter E vs Froude number ($\mathrm{Fr} = \sqrt{\mathrm{Ri}_0^{-1}}$) along segments 1–4 from modeled Red Sea northern channel simulation (dotted curves), from Mediterranean Sea outflow observations (from Fig. 7b in Baringer and Price 1997b; only the mean values are marked with ×), and from laboratory experiments by Ellison and Turner [1959; Eq. (13), marked with asterisks] and laboratory experiments by others [Lofquist 1960; Turner 1973; Fernando 1991; Eq. (14), marked with ''crosses''].

from a nonhydrostatic model with sufficient resolution ($\Delta x = 73$ m, $\Delta z = 9$ m, $\Delta t = 1$ s) to capture various details of overflow instability, mixing and entrainment, and internal waves.

The evolution of the numerical simulation can be divided into two stages. The first stage is characterized by the propagation of the density front across the domain and the second by a statistical equilibrium. The timescale to reach an equilibrium is determined by the advection time of the highest salinity and temperature water masses near the bottom, which is several times longer than the propagation time of the initial front because of smaller velocities near the bottom. At the equilibrium state, the model temperature and salinity distributions are compared to those from REDSOX-1 data and are found to show good agreement on the general characteristics of the system: (i) the gradual thickening of the overflow with downslope distance, with pronounced increase in thickness in the bowl between Station 81 and 38; (ii) the advection of high salinity and temperature signals at the bottom layer throughout the channel with little dilution; and (iii) ambient water masses sandwiched between the overflow and surface mixed layer. A quantitative comparison of the model results with REDSOX-1 station profiles shows that rms errors are reasonably small (≤16%) and are uniform for both salinity and temperature at all stations. The primary deviation of the model from observations is found to be located near the bottom. These errors appear to be related in part to observational profile of the overflow plume at the inlet to the domain, which could include sampling errors, or effects of time dependence (e.g., tides) and three-dimensionality (e.g., edge effects from channel walls).

To quantify the mixing of the overflow with the ambient fluid, entrainment is estimated based on the transport increase along the slope. At first order, the entrainment parameter is found to depend linearly on the characteristic slope angle $\overline{\theta}$ of topographic segments. The descent speed of the overflow and bulk Richardson numbers Ri_0 also compare well between the model and observations. Based on model results, the relationship between the entrainment parameter and bulk Richardson number Ri_0 is also investigated, and the nature and range of such relationship are found to be in reasonable agreement with those reported from various laboratory experiments (Lofquist 1960; Fernando 1991; Turner 1986) and that based on measurements of the Mediterranean overflow (Baringer and Price 1997b).

While the results from this study show various agreements with previous notions on the dynamics of the overflows, it also gives a clear sense of how complicated these dynamics can be. The numerical simulation displays large variability due to various internal waves. Such phenomena, as well as others, will be topics of further investigation. The impact of the change in input buoyancy flux and ambient stratification on overflow dynamics and entrainment will be investigated using REDSOX-2 (summer) dataset. The domain will be extended to simulate the separation of the overflow from the bottom and the details of processes that determine the product water masses. To conclude, further investigation of the rich and complex dynamics of overflows using dedicated, process-oriented studies appears to be an essential step toward the ultimate goal of enhancing the reliability of large-scale oceanic and climate simulations.

Acknowledgments. T. M. Özgökmen greatly appreciates the support the Office of Naval Research Grant N00014-01-1-0023 and National Science Foundation Grant DMS 0209326. W. Johns and H. Peters greatly appreciate the support of the National Science Foundation Grant OCE 98-9819506. The authors thank A. Bower, J. Price, R. Hallberg, C. Rooth, and E. Özsoy for valuable comments and discussions.

REFERENCES

Arakawa, A., 1966: Computational design for long-term numerical integration of the equations of fluid motion: Two dimensional incompressible flow. Part I. *J. Comput. Phys.*, **1,** 119–143.

Baines, P. G., 2001: Mixing in flows down gentle slopes into stratified environments. *J. Fluid Mech.*, **443,** 237–270.

Baringer, M. O., and J. F. Price, 1997a: Mixing and spreading of the Mediterranean outflow. *J. Phys. Oceanogr.*, **27,** 1654–1677.

——, and ——, 1997b: Momentum and energy balance of the Mediterranean outflow. *J. Phys. Oceanogr.*, **27,** 1678–1692.

Beckmann, A., 1998: The representation of bottom boundary layer processes in numerical ocean circulation models. *Ocean Modeling and Parameterization,* E. P. Chassignet and J. Verron, Eds., Kluwer, 135–154.

——, and R. Döscher, 1997: A method for improved representation of dense water spreading over topography in geopotential-coordinate models. *J. Phys. Oceanogr.*, **27,** 581–591.

Borenäs, K. M., and P. A. Lundberg, 1988: On the deep-water flow through the Faroe Bank Channel. *J. Geophys. Res.,* **93,** 1281–1292.

Bower, A. S., H. D. Hunt, and J. F. Price, 2000: Character and dynamics of the Red Sea and Persian Gulf outflows. *J. Geophys. Res.,* **105,** 6387–6414.

——, D. M. Fratantoni, W. E. Johns, and H. Peters, 2002: Gulf of Aden eddies and their impact on Red Sea Water. *Geophys. Res. Lett.,* **29,** 2025, doi:10.1029/2002GL015342.

Britter, R. E., and J. E. Simpson, 1978: Experiments on the dynamics of a gravity current head. *J. Fluid Mech.,* **88,** 223–240.

——, and P. F. Linden, 1980: The motion of the front of a gravity current traveling down an incline. *J. Fluid Mech.,* **99,** 531–543.

Bryden, H. L., and T. H. Kinder, 1991: Steady two-layer exchange through the Strait of Gibraltar. *Deep-Sea Res.,* **38** (Suppl.), S445–S463.

Dickson, R. R., E. M. Gmitrowics, and A. J. Watson, 1990: Deep water renewal in the northern North Atlantic. *Nature,* **344,** 848–850.

Ellison, T. H., and J. S. Turner, 1959: Turbulent entrainment in stratified flows. *J. Fluid Mech.,* **6,** 423–448.

Fedorov, K. N., and S. L. Meschanov, 1988: Structure and propagation of Red Sea waters in the Gulf of Aden. *Okeanologiya,* **28,** 357–363.

Fernando, H. J. S., 1991: Turbulent mixing in stratified fluids. *Annu. Rev. Fluid Mech.,* **23,** 455–493.

Flierl, G. R., M. E. Stern, and J. A. Whitehead, 1981: The physical significance of modons: Laboratory experiments and general integral constraints. *Dyn. Atmos. Oceans,* **7,** 233–263.

Gawarkiewicz, G., and D. C. Chapman, 1995: A numerical study of dense water formation and transport on a shallow, sloping continental shelf. *J. Geophys. Res.,* **100C,** 4489–4507.

Gazdag, J., 1976: Time-differencing schemes and transform methods. *J. Comput. Phys.,* **20,** 196–207.

Hacker, J., P. F. Linden, and S. B. Dalziel, 1996: Mixing in lock-release gravity currents. *Dyn. Atmos. Oceans,* **24,** 183–195.

Hallberg, R., 2000: Time integration of diapycnal diffusion and Richardson number–dependent mixing in isopycnal coordinate ocean models. *Mon. Wea. Rev.,* **128,** 1402–1419.

Hallworth, M. A., H. E. Huppert, J. C. Phillips, and S. J. Sparks, 1996: Entrainment into two-dimensional and axisymmetric turbulent gravity currents. *J. Fluid Mech.,* **308,** 289–311.

Härtel, C., E. Meiburg, and F. Necker, 2000: Analysis and direct numerical simulation of the flow at a gravity-current head. Part 1. Flow topology and front speed for slip and no-slip boundaries. *J. Fluid Mech.,* **418,** 189–212.

Huppert, H. E., 1982: The propagation of two-dimensional and axisymmetric viscous gravity currents over a rigid horizontal surface. *J. Fluid Mech.,* **121,** 43–58.

Jia, Y., 2000: On the formation of an Azores Current due to Mediterranean overflow in a modeling study of the North Atlantic. *J. Phys. Oceanogr.,* **30,** 2342–2358.

Jiang, L., and R. W. Garwood Jr., 1995: A numerical study of three-dimensional dense bottom plumes on a Southern Ocean continental slope. *J. Geophys. Res.,* **100,** 18 471–18 488.

——, and ——, 1996: Three-dimensional simulations of overflows on continental slopes. *J. Phys. Oceanogr.,* **26,** 1214–1233.

——, and ——, 1998: Effects of topographic steering and ambient stratification on overflows on continental slopes: A model study. *J. Geophys. Res.,* **103,** 5459–5476.

Johns, W., H. Peters, A. S. Bower, and D. M. Fratantoni, 2002: Red Sea Outflow Experiment (REDSOX): New observations of the descent and spreading of the Red Sea water. *Eos, Trans. Amer. Geophys. Union,* **83,** OS319.

Jungclaus, J. H., and J. O. Backhaus, 1994: Application of a transient reduced gravity plume model to the Denmark Strait Overflow. *J. Geophys. Res.,* **99,** 12 375–12 396.

——, and G. Mellor, 2000: A three-dimensional model study of the Mediterranean outflow. *J. Mar. Syst.,* **24,** 41–66.

Keulegan, G. H., 1958: The motion of saline fronts in still water. U.S. National Bureau of Standards Rep. 5831, 29 pp.

Killworth, P. D., 1977: Mixing on the Weddell Sea continental slope. *Deep-Sea Res.,* **24,** 427–448.

——, and N. R. Edwards, 1999: A turbulent bottom boundary layer code for use in numerical ocean models. *J. Phys. Oceanogr.,* **29,** 1221–1238.

Large, W., 1998: Modeling and parameterizing ocean planetary boundary layers. *Ocean Modeling and Parameterization*, E. P. Chassignet and J. Verron, Eds., Kluwer, 81–120.

Lesieur, M., 1997: *Turbulence in Fluids.* 3d ed. Kluwer, 515 pp.

Lofquist, K., 1960: Flow and stress near an interface between stratified liquids. *Phys. Fluids,* **3,** 158–175.

Lozier, M. S., W. B. Owens, and R. G. Curry, 1995: The climatology of the North Atlantic. *Progress in Oceanography,* Vol. 36, Pergamon, 1–44.

Marmorino, G. O., 1987: Observations of small-scale mixing processes in the seasonal thermocline. Part II: Wave breaking. *J. Phys. Oceanogr.,* **17,** 1348–1355.

Meleshko, V. V., and G. J. F. van Heijst, 1995: Interacting two-dimensional vortex structures: Point vortices, contour kinematics and stirring properties. *Chaos Applied to Fluid Mixing,* H. Aref and M. S. El Naschie, Eds., Pergamon, 233–266.

Mellor, G. L., and T. Yamada, 1982: Development of a turbulence closure model for geophysical fluid problems. *Rev. Geophys. Space Phys.,* **20,** 851–875.

Millero, F. J., G. Perron, and J. E. Desnoyers, 1976: The density of sea-water solutions as a function of temperature and salinity. *J. Mar. Res.,* **34,** 61–93.

Monaghan, J. J., R. A. F. Cas, A. M. Kos, and M. Hallworth, 1999: Gravity currents descending a ramp in a stratified tank. *J. Fluid Mech.,* **379,** 39–70.

Morcos, S. A., 1970: Physical and chemical oceanography of the Red Sea. *Oceanogr. Mar. Biol.,* **8,** 73–202.

Morton, B. R., G. I. Taylor, and J. S. Turner, 1956: Turbulent gravitational convection from maintained and instantaneous sources. *Proc. Roy. Soc. London,* **A234,** 1–23.

Murray, S. P., and W. E. Johns, 1997: Direct observations of seasonal exchange through the Bab el Mandab Strait. *Geophys. Res. Lett.,* **24,** 2557–2560.

Nakano, H., and N. Suginohara, 2002: Effects of bottom boundary layer parameterization on reproducing deep and bottom waters in a world ocean model. *J. Phys. Oceanogr.,* **32,** 1209–1227.

Nielsen, A. H., and J. J. Rasmussen, 1996: Formation and temporal evolution of the Lamb-dipole. *Phys. Fluids,* **9,** 982–991.

Özgökmen, T. M., and O. E. Esenkov, 1998: Asymmetric salt fingers induced by a nonlinear equation of state. *Phys. Fluids,* **10,** 1882–1890.

——, and F. Crisciani, 2001: On the dynamics of β plumes. *J. Phys. Oceanogr.,* **31,** 3569–3580.

——, and E. Chassignet, 2002: Dynamics of two-dimensional turbulent bottom gravity currents. *J. Phys. Oceanogr.,* **32,** 1460–1478.

——, O. E. Esenkov, and D. B. Olson, 1998: A numerical study of layer formation due to fingers in double-diffusive convection in a vertically bounded domain. *J. Mar. Res.,* **56,** 463–487.

——, E. P. Chassignet, and C. G. H. Rooth, 2001: On the connection between the Mediterranean outflow and the Azores Current. *J. Phys. Oceanogr,* **31,** 461–480.

Özsoy, E., D. D. Iorio, M. C. Gregg, and J. O. Backhaus, 2001: Mixing in the Bosphorus Strait and the Black Sea continental shelf: Observations and a model of the dense outflow. *J. Mar. Syst.,* **31,** 99–135.

Papadakis, M. P., E. P. Chassignet, and R. W. Hallberg, 2003: Numerical simulations of the Mediterranean Sea outflow: Impact of the entrainment parameterization in an isopycnic coordinate ocean model. *Ocean Modell.,* in press.

Peters, H., W. Johns, and S. Matt, 2002: Red Sea Outflow Experiment (REDSOX): Turbulence and mixing and the descending plume. *Eos, Trans. Amer. Geophys. Union,* **83,** OS320.

Price, J. F., and M. O. Baringer, 1994: Outflows and deep water production by marginal seas. *Progress in Oceanography*, Vol. 33, Pergamon, 161–200.

——, and J. Yang, 1998: Marginal sea overflows for climate simulations. *Ocean Modeling and Parameterization,* E. P. Chassignet and J. Verron, Eds., Kluwer, 155–170.

——, and Coauthors, 1993: Mediterranean outflow mixing and dynamics. *Science,* **259,** 1277–1282.

Siedler, G., 1969: General circulation of the water masses in the Red Sea. *Hot Brines and Recent Heavy Metal Deposits in the Red Sea,* E. T. Degens and D. A. Ross, Eds., Springer-Verlag, 131–137.

Simpson, J. E., 1969: A comparison between laboratory and atmospheric density currents. *Quart. J. Roy. Meteor. Soc.*, **95,** 758–765.

——, 1982: Gravity currents in the laboratory, atmosphere, and the ocean. *Annu. Rev. Fluid Mech.,* **14,** 213–234.

——, 1987: *Gravity Currents in the Environment and the Laboratory*. John Wiley and Sons, 244 pp.

——, and R. E. Britter, 1979: The dynamics of the head of a gravity current advancing over a horizontal surface. *J. Fluid Mech.,* **94,** 477–495.

Smith, P. C., 1975: A streamtube model for bottom boundary currents in the ocean. *Deep-Sea Res.*, **22,** 853–873.

Smith, R. A., 1991: Maximization of vortex entropy as an organizing principle in intermittent, decaying, two-dimensional turbulence. *Phys. Rev.*, **A43,** 1126–1129.

Sofianos, S. S., W. E. Johns, and S. P. Murray, 2002: Heat and freshwater budgets in the Red Sea from direct observations at Bab el Mandeb. *Deep-Sea Res.*, **49B,** 1323–1340.

Swarztrauber, P. N., 1977: The methods of cyclic reduction, Fourier analysis and FACR algorithm for discrete solution of the Poisson equation an a rectangle. *SIAM Rev.,* **19,** 490–501.

Turner, J. S., 1962: The starting plume in neutral surroundings. *J. Fluid Mech.,* **13,** 356–368.

——, 1973: *Buoyancy Effects in Fluids.* Cambridge University Press, 367 pp.

——, 1986: Turbulent entrainment: The development of the entrainment assumption, and its applications to geophysical flows. *J. Fluid Mech.,* **173,** 431–471.

Willebrand, J., and Coauthors, 2001: Circulation characteristics in three eddy-permitting models of the North Atlantic. *Progress in Oceanography*, Vol. 48, Pergamon, 123–161.

Winton, M., R. Hallberg, and A. Gnanadesikan, 1998: Simulation of density-driven frictional downslope flow in *Z*-coordinate ocean models. *J. Phys. Oceanogr.,* **28,** 2163–2174.